

AD-A260 129



①

CHARACTERIZATION OF MECHANICAL DAMAGE MECHANISMS IN CERAMIC AND POLYMERIC MATRIX COMPOSITE MATERIALS

By
James Lankford, Jr.

DTIC
ELECTE
JAN 26 1993
S c D

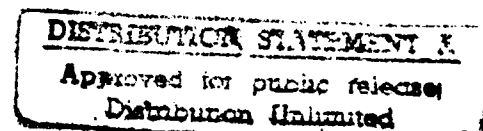
TECHNICAL REPORT
ONR Contract No. N00014-92-C-0093
ONR Contract Authority NR 032-553
SwRI Project 06-5035

Prepared For
Office of Naval Research
Arlington, VA 22217
By
Southwest Research Institute
San Antonio, Texas

93-01375



December 1992



Reproduction in whole or in part is permitted for any purpose of the United States Government



SOUTHWEST RESEARCH INSTITUTE
SAN ANTONIO
DETROIT
HOUSTON
WASHINGTON, DC

SECURITY CLASSIFICATION OF THIS PAGE

REPORT DOCUMENTATION PAGE

Form Approved
OMB No. 0704-0188
Exp. Date: Jun 30, 1986

REPORT SECURITY CLASSIFICATION UNCLASSIFIED		1b. RESTRICTIVE MARKINGS	
SECURITY CLASSIFICATION AUTHORITY		3. DISTRIBUTION/AVAILABILITY OF REPORT	
DECLASSIFICATION/DOWNGRADING SCHEDULE		Distribution Limited	
PERFORMING ORGANIZATION REPORT NUMBER(S) i-5035		5. MONITORING ORGANIZATION REPORT NUMBER(S)	
NAME OF PERFORMING ORGANIZATION Southwest Research Institute	8b. OFFICE SYMBOL (If applicable)	7a. NAME OF MONITORING ORGANIZATION Dr. Steven G. Fishman - Code 431N Office of Naval Research	
ADDRESS (City, State, and ZIP) 2200 Culebra Road, PO Drawer 28510 San Antonio, TX 78228-0510		7b. ADDRESS (City, State, and ZIP Code) 800 North Quincy Street Arlington, VA 22217	
NAME OF FUNDING/SPONSORING ORGANIZATION Office of Naval Research	8b. OFFICE SYMBOL (If applicable)	9. PROCUREMENT INSTRUMENT IDENTIFICATION NUMBER N00014-92-C-0093	
ADDRESS (City, State, and ZIP) 800 North Quincy Street Arlington, VA 22217		10. SOURCE OF FUNDING NUMBERS	
		PROGRAM ELEMENT NO.	PROJECT NO.
		TASK NO.	WORK UNIT ACCESSION NO.
TITLE (Include Security Classification) Characterization of Mechanical Damage Mechanisms in Ceramic and Polymeric Matrix Composite Materials			
PERSONAL AUTHOR(S)			
1. TYPE OF REPORT Technical	13. b TIME COVERED FROM 10/91 TO 10/92	14. DATE OF REPORT (Year, Month, Day) December 1992	15. PAGE COUNT 72
SUPPLEMENTARY NOTATION			
COSATI CODES		18. SUBJECT TERMS (Continue on reverse if necessary and identify by block number)	
FIELD	GROUP	SUB-GROUP	
ABSTRACT (Continue on reverse if necessary and identify by block number) In order to better establish the fundamental mechanisms responsible for the onset of microstructural instability during compressive loading, several fiber-reinforced polymeric matrix composites were tested under conditions involving hydrostatic confinement. It was found that the dependence of strength upon pressure was mild, indicating that the overwhelming factor in the compressive failure of these materials, irrespective of fiber type, matrix, composition, and composite architecture, is resistance to shear loading; dilatational mechanisms, certainly ones associated with microfracture, are relatively insignificant. Specific strength levels do appear to be controlled by both inelastic and elastic flow properties of the matrix, and reflect the degree to which the matrix can restrain either the flexure of locally misaligned fibers, or the shear displacement of non-axial cross-plyed fibers in more complex composite lay-ups. To determine the influence of applied stress anisotropy on composite damage development, the behavior of a unidirectional carbon fiber-reinforced composite was characterized under hydrostatically confined uniaxial and in-plane biaxial compression. The failure process under uniaxial loading was observed to involve kink bands combining into a macroscopic shear band. Incidental interlamellar splitting was observed, its extent decreasing with hydrostatic pressure. The composite was found to exhibit markedly lower in-plane biaxial failure strength in the direction parallel to the fibers when compared to the uniaxial case. It is shown that the origin of the six-fold strength differential between the two situations probably lies in the involvement, via state-of-stress, of two different, specific manifestations of fiber lay-up imperfection. Extending the focus of the effort to brittle composite systems, the influence of hydrostatic confinement on compressive strength and corresponding failure mechanisms was explored for SiC-reinforced glass ceramics tested at different strain rates. Two composite architectures (0° and 0°/90°) were studied, versus monolithic glass ceramic tested under similar conditions. Composite confined pressure results are interpreted in terms of fiber buckling under quasistatic conditions and fiber kinking at high pressures, and compared with monolithic (monocomposite) microfracture coalescence at low pressures versus shear band formation under more intense confinement.			
DISTRIBUTION/AVAILABILITY OF ABSTRACT <input checked="" type="checkbox"/> UNCLASSIFIED/UNLIMITED <input type="checkbox"/> SAME AS RPT. <input type="checkbox"/> DTIC USERS		21. ABSTRACT SECURITY CLASSIFICATION UNCLASSIFIED	
3. NAME OF RESPONSIBLE INDIVIDUAL James Lankford		22b. TELEPHONE (Include Area Code) 210/522-5122	22c. OFFICE SYMBOL

UNCLASSIFIED

ABSTRACT (Continued)

Certain high strain rate damage modes in brittle composites appear to derive from the behavior of the matrix phase alone. Consequently, the split Hopkinson pressure bar was used to characterize the failure of a high strength alumina at strain rates well in excess of 10^3 sec^{-1} . There appears to be a critical strain rate above which the traditional method of using the transmitter bar material to calculate the stress in the specimen is no longer valid. To compute the correct stress in the specimen it is necessary to use the strain signal from gages mounted directly on the specimen, a procedure which must be incorporated into higher loading rate extrapolations of the present work involving composites.

Accession For

NTIS GRA&I	<input checked="checked" type="checkbox"/>
DTIC TAB	<input type="checkbox"/>
Unannounced	<input type="checkbox"/>
Justification	

By _____

Distribution/ _____

Availability Codes

Dist	Avail and/or	Special
A-1		

UNCLASSIFIED

FOREWARD

This report consists of four papers submitted for publication in the journals noted on the title pages. Some of the work represents collaborative effort between researchers at Southwest Research Institute, Michigan Technical University, and the Commission of the European Communities Joint Research Centre, Ispra, Italy.

TABLE OF CONTENTS

	<u>Page</u>
I. THE COMPRESSIVE FAILURE OF POLYMERIC COMPOSITES UNDER HYDROSTATIC CONFINEMENT	1
II. FAILURE MECHANISMS IN A UNIDIRECTIONAL FIBER-REINFORCED THERMOPLASTIC COMPOSITE UNDER UNIAXIAL, IN-PLANE BIAXIAL, AND HYDROSTATICALLY CONFINED COMPRESSION	27
III. THE EFFECT OF HYDROSTATIC PRESSURE AND LOADING RATE ON COMPRESSIVE FAILURE OF FIBER-REINFORCED CERAMIC MATRIX COMPOSITES	40
IV. TESTING OF HIGH STRENGTH CERAMICS WITH THE SPLIT HOPKINSON PRESSURE BAR	62

LIST OF FIGURES

<u>Figure</u>		<u>Page</u>
I.		
THE COMPRESSIVE FAILURE OF POLYMERIC COMPOSITES UNDER HYDROSTATIC CONFINEMENT		
1	Schematic of confined pressure test setup.	4
2	Compressive stress-strain behavior of 0° graphite/PEEK for various confining pressures.	7
3	Compressive true stress-true strain behavior of PEEK for various confining pressures.	9
4	Compressive stress-strain behavior of 90° E-glass/epoxy and neat epoxy for various confining pressures.	10
5	Compressive strength versus confining pressure for composite variants.	11
6	Flow stress versus confining pressure for matrix materials.	12
7	Initial elastic modulus versus confining pressure for matrix materials.	13
8	Macroscopic composite failure modes.	15
9	Kink details in 0° graphite/PEEK.	16
10	Shear damage mechanisms in 0°/90° E-glass/PEEK.	17
11	Shear damage development in 0°/90° E-glass/PEEK AT $\Sigma_3 = 150$ MPa.	19
12	Shear failure in confined 90° E-glass/epoxy, showing absence of bulk damage otherwise.	20
13	Pressure dependence of failure strength for uniaxially-reinforced graphite/PEEK and graphite/epoxy, compared with pressure dependence of flow stress for pure polymer matrices.	21
II.		
THE COMPRESSIVE FAILURE OF POLYMERIC COMPOSITES UNDER HYDROSTATIC CONFINEMENT		
1	Compression specimen configurations.	29
2	Engineering stress-strain response in the fiber direction for uniaxial and biaxial experiments.	32
3	Engineering stress-strain response in the two loading directions for the biaxial experiment.	32
4	Section of uniaxial specimen tested at a confining pressure of 250 MPa.	34

LIST OF FIGURES (Cont'd.)

Figure		Page
5	Section of uniaxial specimen tested under ambient pressure.	35
6	Biaxial damage development.	37
7	Schematic of compressive sequence; $V_1 \gg V_2$.	39

III. THE EFFECT OF HYDROSTATIC PRESSURE AND LOADING RATE ON COMPRESSIVE FAILURE OF FIBER-REINFORCED CERAMIC MATRIX COMPOSITES

1	Schematic of stress distribution related to combined hydrostatic pressure– compression testing.	42
2	Dimensions and orientations of cross-ply bundles and fibers.	44
3	Schematic of compression test setup.	46
4	Axial stress versus strain for matrix material.	48
5	Axial stress versus strain for $0^\circ/90^\circ$ composite.	49
6	Axial stress versus strain for uniaxially reinforced composite.	50
7	Compressive strength of pyroceramic versus confining pressure.	52
8	Compressive strength of $0^\circ/90^\circ$ composite versus confining pressure.	53
9	Compressive strength of 0° composite versus confining pressure.	54
10	Compressive failure of pyroceramic, showing shear band formation; $\dot{\epsilon} = 10^{-4} \text{ s}^{-1}$, $\sigma_3 = 200 \text{ MPa}$ (σ_1 vertical).	55
11	Compressive failure of $0^\circ/90^\circ$ composite; $\dot{\epsilon} = 10^{-4} \text{ s}^{-1}$, $\sigma_3 = 0$ (σ_1 vertical).	56
12	Compressive failure modes of composites; $\dot{\epsilon} = 10^{-4} \text{ s}^{-1}$, $\sigma_3 = 50 \text{ MPa}$, σ_1 vertical.	57

IV. TESTING OF HIGH STRENGTH CERAMICS WITH THE SPLIT HOPKINSON PRESSURE BAR

1	Schematic diagram of split Hopkinson pressure bar.	63
2	Compressive stress and strain signals from SHPB test of MTU alumina.	66
3	Compressive stress and strain signals from SHPB test of MTU alumina.	66

LIST OF FIGURES (Cont'd.)

<u>Figure</u>		<u>Page</u>
4	Comparison of stress-derived strain and specimen strain gage signal for the low strain rate test of Figure 2.	67
5	Comparison of stress-derived strain and specimen strain gage signal for the high strain rate test of Figure 3.	68
6	Comparison of specimen gage-derived strain rates and stress-derived strain rates for a number of tests.	69

(Submitted to *Composites*)

I.

**THE COMPRESSIVE FAILURE OF POLYMERIC
COMPOSITES UNDER HYDROSTATIC CONFINEMENT**

by

**J. Lankford
Southwest Research Institute
San Antonio, TX 78228**

ABSTRACT

In order to better establish the fundamental mechanisms responsible for the onset of microstructural instability during compressive loading, several fiber-reinforced polymeric matrix composites were tested under conditions involving hydrostatic confinement. It was found that the dependence of strength upon pressure was mild, indicating that the overwhelming factor in the compressive failure of these materials, irrespective of fiber type, matrix, composition, and composite architecture, is resistance to shear loading; dilatational mechanisms, certainly ones associated with microfracture, are relatively insignificant. Specific strength levels do appear to be controlled by both inelastic and plastic flow properties of the matrix, and reflect the degree to which the matrix can restrain either the flexure of locally misaligned fibers, or the shear displacement of non-axial cross-plyed fibers in more complex composite lay-ups.

I. INTRODUCTION

Fiber-reinforced polymeric composites are notorious for their susceptibility to compressive failure. In bending, for example, failure often initiates on the compressive side of the specimen. Compression of these materials has received both theoretical¹⁻⁴ and experimental⁵⁻¹⁰ study, and it is clear that: (1) the failure process usually is unstable, which makes it hard to see how it begins; (2) overall instability is triggered within a highly localized region; (3) this local instability (inter-lamellar splitting, fiber buckling, disbonding, shearing, kinking) is controlled by a number of factors, including matrix strength and elastic properties; fiber strength, modulus, and degree of alignment; and the degree of overall restraint imposed on the system.

Recent work^{1-4,7} has emphasized the crucial role of initial fiber misalignment in promoting local stress amplification, and it has been shown that regardless of the specific failure modes (extension, kinking, tensile fiber fracture) or mode of matrix deformation (elastic or inelastic), such misalignment lowers the uniaxial compressive strength significantly versus the theoretical value predicted by Rosen's classic theory¹¹ for perfectly aligned fibers. However, there remains the question, given that some misalignment probably will always exist, of the material response engendered by this factor. A number of analyses maintain that instability may occur under elastic conditions,^{3,4} *i.e.*, matrix yielding is not necessary, while others^{1,2,7} propose that inelastic or even true plastic¹² matrix deformation is required. Regardless, fiber fracture must be accommodated by either extensional (dilatational) or shear (nondilatational) matrix deformation.

A powerful means of separating such modes is to conduct tests under varying degrees of hydrostatic confinement, which tends to inhibit dilatational mechanisms. In earlier work by Weaver and Williams,¹³ carbon fiber-reinforced epoxy matrix composites were subjected to compression under superimposed hydrostatic pressure. It was observed that the axial splitting which accompanies compressive failure under ambient conditions was suppressed, and only shear/kink modes were permitted. However, associated with increasing pressure was a rapid rise in strength,

which was interpreted in terms of pre-kink fiber-matrix tensile fracture, *i.e.*, a pressure-sensitive dilatational mechanism, occurring in the transverse direction at the site of buckled fibers. A large body of work¹⁴⁻¹⁶ has shown that polymers themselves possess a significant pressure sensitivity, although the matrix contribution to the overall strength of the composite is low if considered purely in terms of its axial component of stress. Generally, the compressive yield strengths of both crystalline and amorphous polymers have been observed to increase with confinement, but not as robustly as that measured by Weaver and Williams¹³ for polymeric composites.

In the present study, matrices (thermoset versus thermoplastic), fibers (E-glass versus carbon fiber) and composite architectures (0°, 90°, 0°/90°) are varied. Hydrostatic confinement is employed as a means of inferring the relative roles of dilatational versus shear microfailure mechanisms.

II. EXPERIMENTAL FACTORS

Materials

Several composites were selected for study; relevant microstructural details are given in Table I. Also included were neat versions of the semi-crystalline PEEK and the epoxy matrix materials.

Specimen Design

Cylindrical specimens 1.2 cm long x 0.6 cm diameter, with a slightly reduced midsection (Figure 1), were machined from sample blanks and their ends ground parallel to within 2 μ m tolerance. Earlier work¹⁸ has verified that this specimen configuration produces compressive strengths equal to or greater than those obtained using standard tabbed panel configurations;

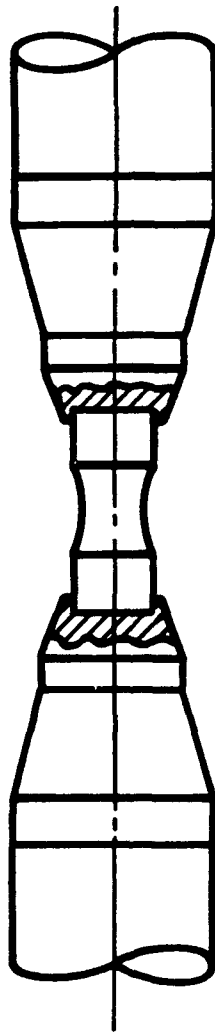


FIGURE 1. Schematic of confined pressure test setup.

moreover, a cylindrical design is imperative for hydrostatic confinement. The compression test axis was parallel and normal to the fibers for the 0° and 90° samples, respectively, while for the 0°/90° material, the load axis was oriented parallel to the 0° direction.

TABLE I.
COMPOSITE MATERIALS

Lay-up	Fiber	Fiber Diameter (μm)	Fiber Volume (%)	Matrix
uniaxial	PAN graphite*	7	60	PEEK (standard semi-crystalline condition)
uniaxial	E-glass	15	55	epoxy**
0°/90°	E-glass	15	60	PEEK (amorphous***)

* AS4

** Epon 828

*** DuPont J2

To prevent brooming of the composites, and ensure valid gage section failure, their ends were constrained using caps of high-strength steel; the slight gap between the caps and the specimens was filled with epoxy. Transition between the specimen and the load ram was provided by a conical shaped alumina platen; the entire load train is shown in Figure 1. To prevent infiltration by the silicone-based pressure fluid during confined pressure testing, samples were sealed within thin, heat-shrinkable Teflon tubing, overlapping the ends of the platens.

Test Procedures

Controlled strain rate tests were performed at approximately 10^{-4} s^{-1} , with a servo-controlled hydraulic ram supplying the axial load. For tests with radial confining pressure, a special pressure vessel was utilized. In performing the experiments, the hydrostatic pressure was first raised to the

desired level by pumping fluid into the pressure vessel while a servo-controller matched the axial stress to the pressure. The axial load was then increased under displacement control at fixed pressure. A bridge of four electrical resistance strain gages inside the pressure vessel measured the axial load. Since the hydrostatic pressure produced a zero shift in the output of this load cell, the magnitude of the shift was measured in a series of calibration runs and subtracted from the load measurements. Hydrostatic pressure was measured by a diaphragm-type electrical pressure transducer located at the fluid inlet orifice of the pressure vessel. All samples were tested at room temperature, under confining pressures as high as 250 MPa.

Following testing, both partially damaged and totally failed specimens were examined optically while still contained within their transparent Teflon overcoats. Since the experiments were performed under displacement control with radial confinement throughout, even failed specimens remained largely intact. On the other hand, they often fragmented if the coating was removed. In order to prepare the samples for scanning electron microscopy (SEM), a small "window" was cut into the Teflon; under vacuum, epoxy mounting resin was able to infiltrate inside the coating, enter the fragmented damage zone, and seal it in place for diamond saw sectioning. These sections were polished, and coated with palladium for SEM study.

III. RESULTS

Mechanical Behavior

Typical stress*-strain curves as a function of pressure for the graphite/PEEK composite are shown in Figure 2. The effect of confinement is to engender an increase in modulus and yield strength, while failure is catastrophic. Efforts to stop a test at the point of instability, by slowing the rate of loading and monitoring acoustic emission, proved ineffectual.

* Here $\sigma_1 - \sigma_3$ is the axial stress deviator from the initial hydrostatically loaded state, where $\sigma_1 = \sigma_2 = \sigma_3$.

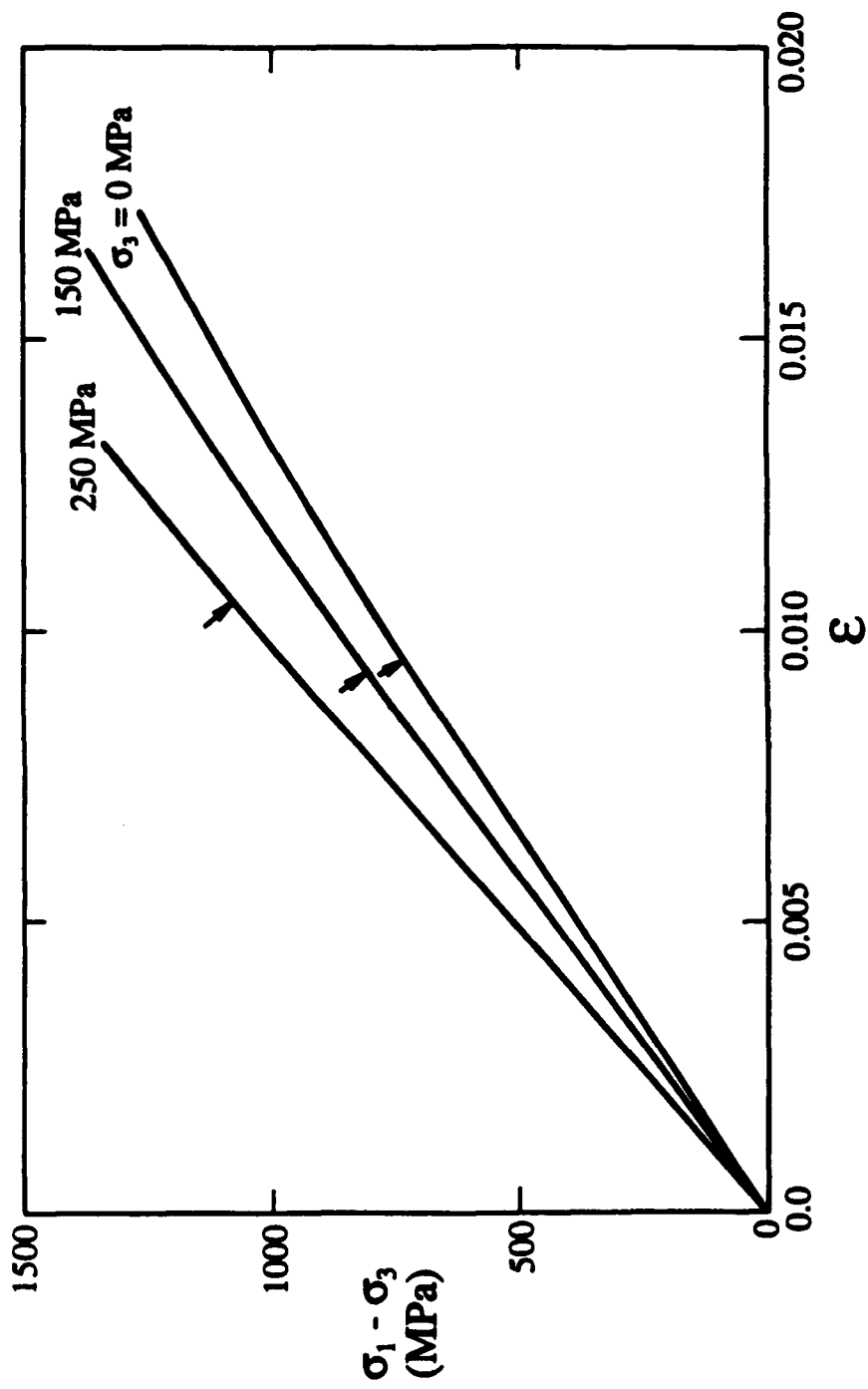


FIGURE 2. Compressive stress-strain behavior of 0° graphite/PEEK for various confining pressures; arrows indicate linear elastic yield point.

The neat resin itself, on the other hand, exhibits extensive plastic flow following yielding (Figure 3). Pressure raises the yield point (deviation from linear stress-strain relationship), the modulus, and the flow stress. It is notable that reversible strains as high as 5% are reached prior to the onset of true plastic flow, thanks to the low intrinsic modulus of the polymers.

Deformation behavior of the 0° E-glass/epoxy and the 0°/90° E-glass/PEEK closely resembles that of the 0° graphite/PEEK. Deformation of 90° E-glass/epoxy, however, is intermediate to these general cases, as shown in Figure 4; here strength, modulus, and ductility rise with increasing pressure. For the neat resin, the average flow stress and modulus also rise with pressure, as shown in the same figure. The composite, however, hardens monotonically to its ultimate strength, and then unloads stably before failing catastrophically.

For all the composite variants, the effect of pressure on strength is moderate, as shown in Figure 5. In particular, there is no functional transition between zero confinement and the application of hydrostatic pressure, suggesting that the key mechanisms responsible for damage development are not altered qualitatively by the relative degree of confinement. In the case of the matrix materials, failure does not occur. Therefore, plotted in Figure 6 are families of curves representing the pressure dependence of the flow stress. It should be noted that large matrix strains (as high as 0.05) of an inelastic nature can occur prior to the onset of plastic flow. This is a consequence of the low "elastic" moduli of the matrices, which are just as pressure sensitive (Figure 7) as the flow stress itself.

On the other hand, while the initial yield stress (deviation from the linear elastic load line) has a similar pressure dependence, the "plastic" deformation associated with this effect is virtually negligible compared with the pressure-sensitive inelastic strains associated with the overall low (in)elastic average moduli. Thus, within the pre-plastic flow region, the pressure-induced changes in overall inelastic deformation will greatly dominate any changes in the virtually microplastic flow deriving from elastic to inelastic yielding.

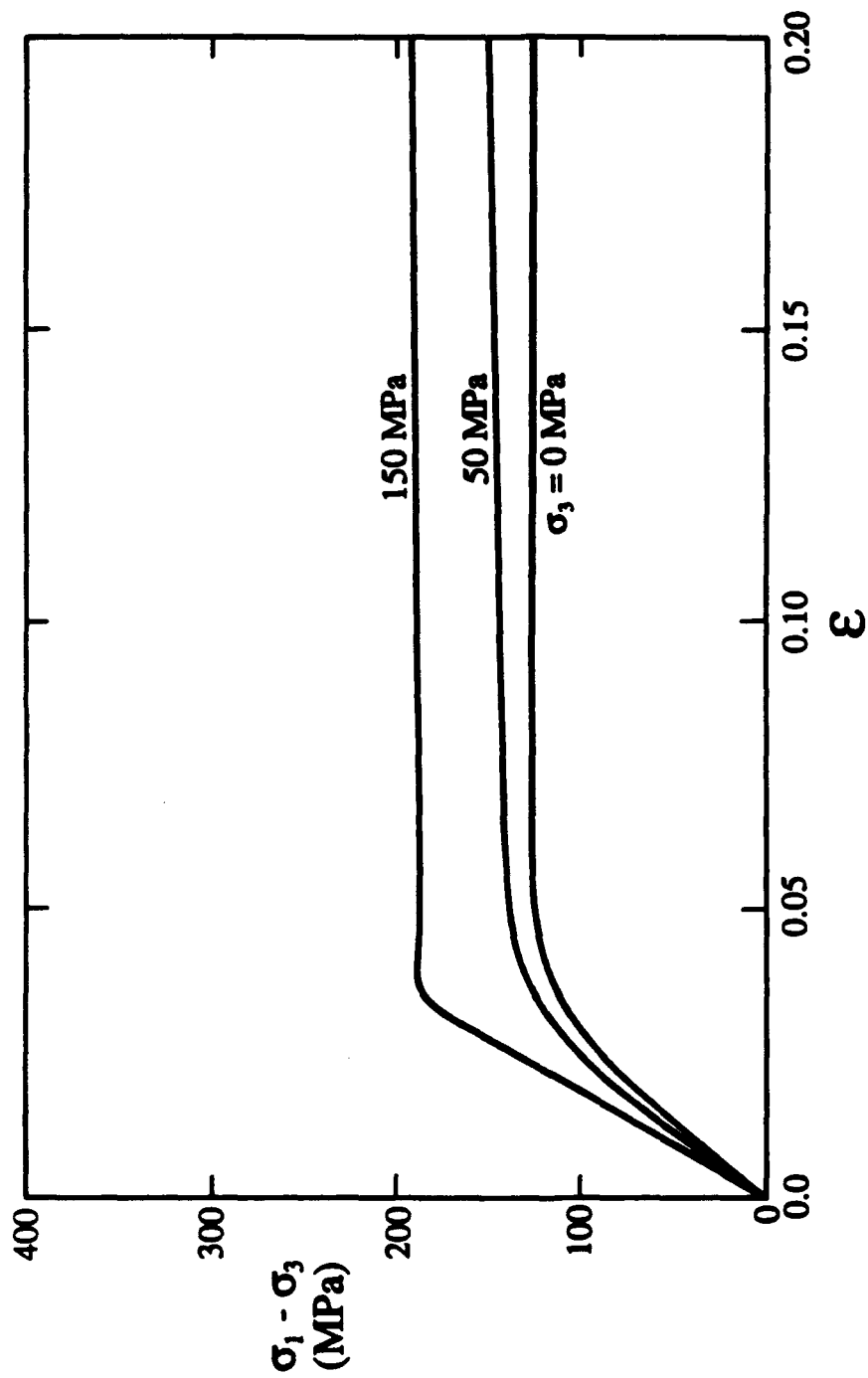


FIGURE 3. Compressive true stress-true strain behavior of PEEK for various confining pressures.

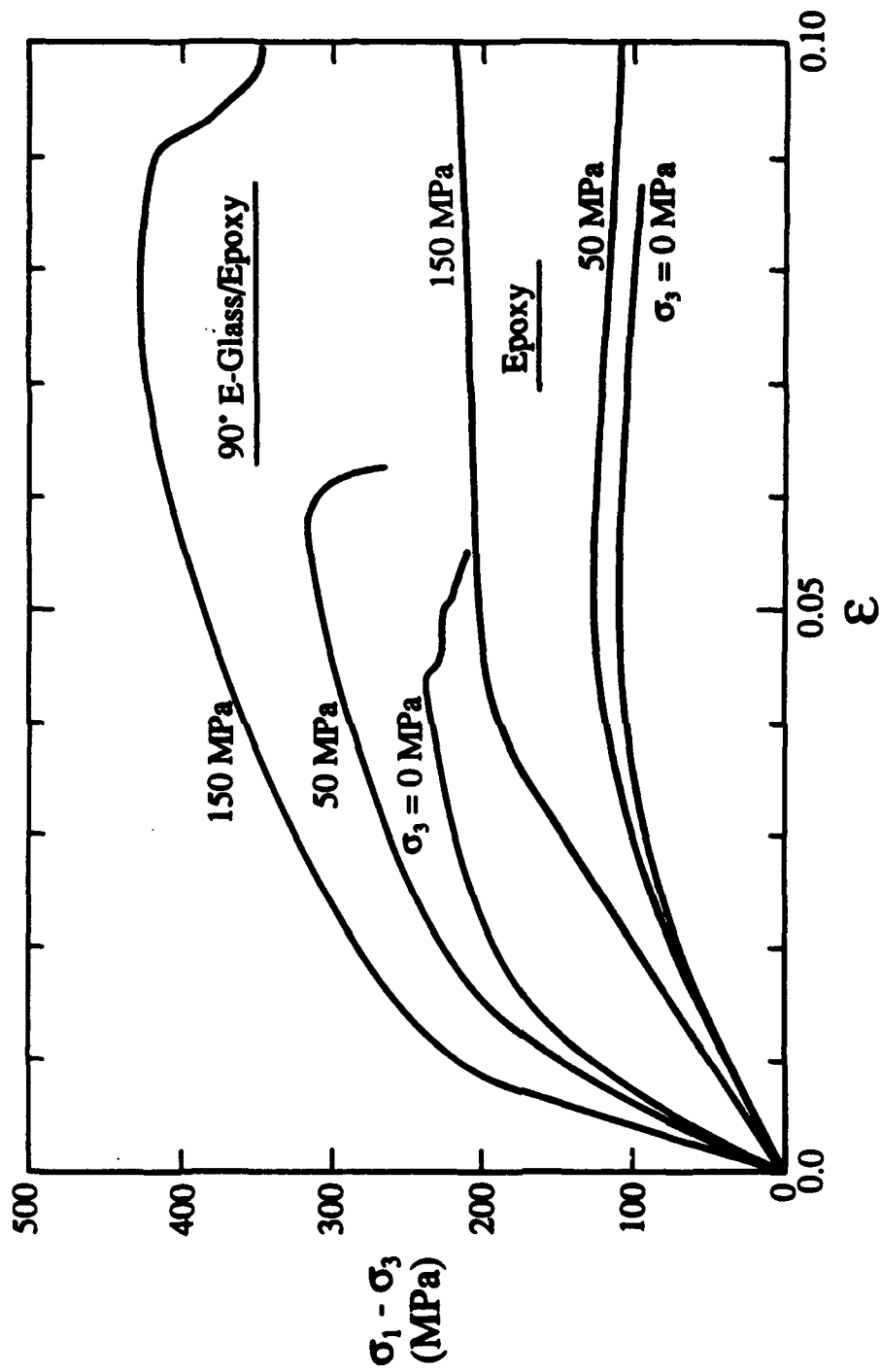


FIGURE 4. Compressive stress-strain behavior of 90° E-glass/epoxy and neat epoxy for various confining pressures.

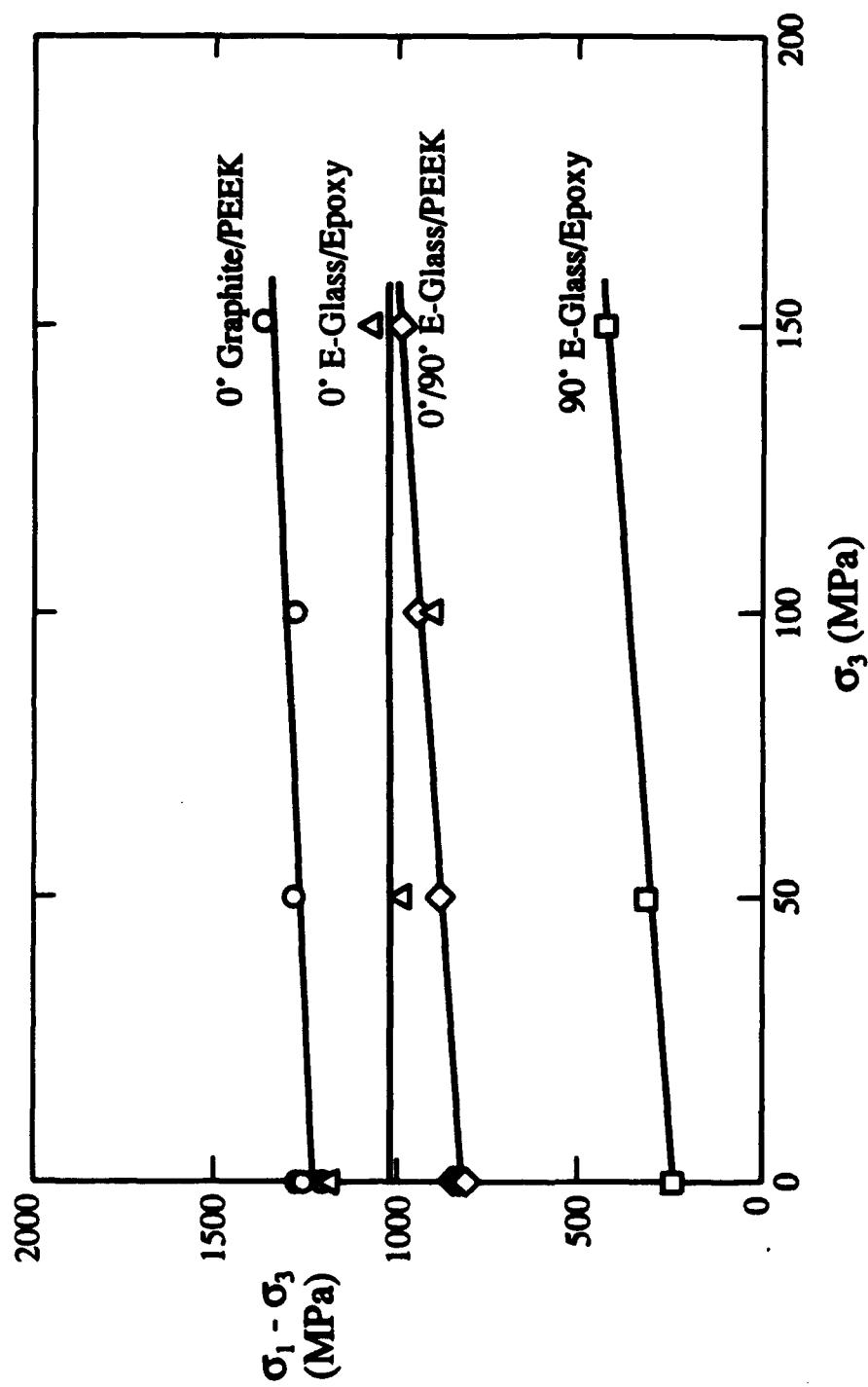


FIGURE 5. Compressive strength versus confining pressure for composite variants.

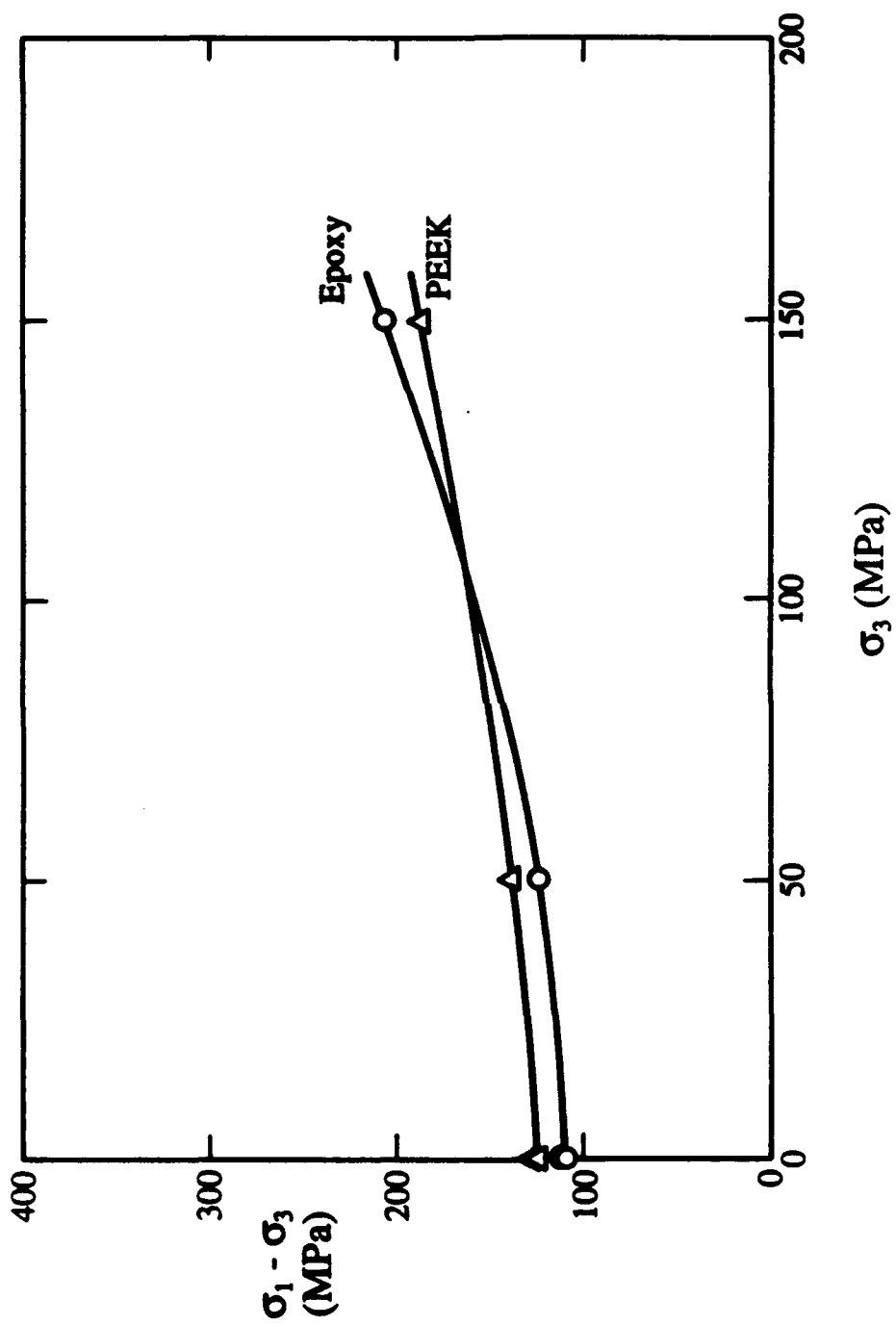


FIGURE 6. Flow stress versus confining pressure for matrix materials.

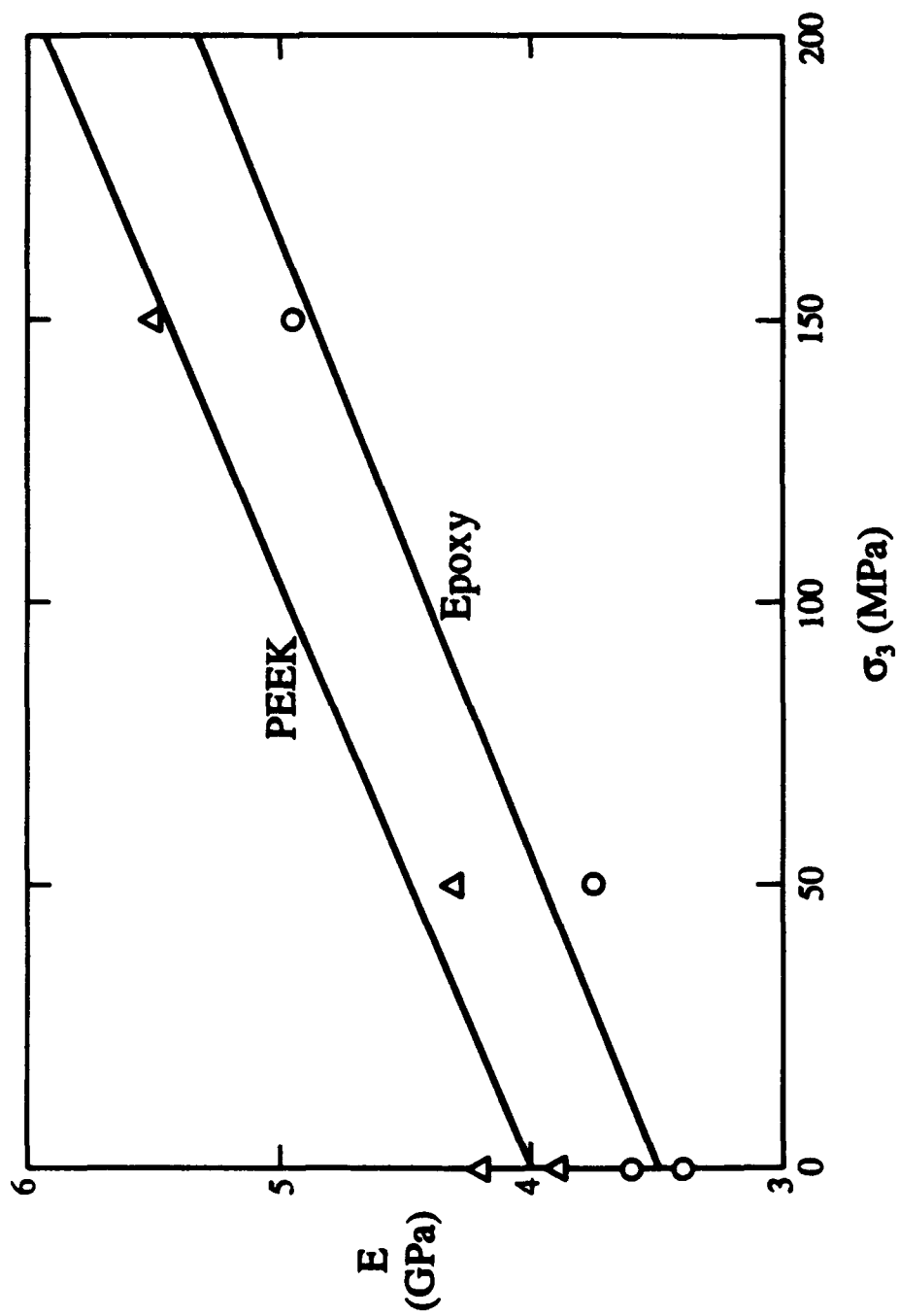


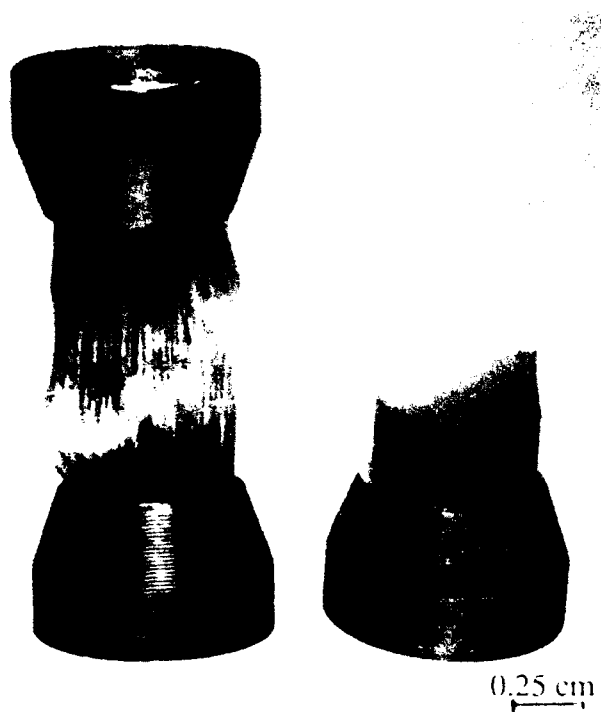
FIGURE 7. Initial elastic modulus versus confining pressure for matrix materials.

Damage Mechanisms

Failure of the various composites is shown macroscopically in Figure 8. Axial splitting was observed extensively only for the 0°/90° laminate in the unconfined state. Higher pressures totally suppressed this damage mode, while shear failure occurred consistently at about 45° for all levels of confinement including $\sigma_3 = 0$ (Figure 8a). The surface of the shear fault shown in the figure consists of a series of stepped ledges, the risers composed of 0° laminates, and the steps being fractures through the 90° sectors. The other composites failed either by classic kinking (both 0° lay-ups, Figure 8b and c) or 45° shear (90° E-glass/epoxy, Figure 8d). In the case of the former materials, the kink angle for both, relative to the stress axis, was approximately 25°, irrespective of confinement. For the 0° lay-ups, failure was confined to the reduced gage sections, while the higher angle shear planes unavoidably extended out of this zone. However, it was possible to stop a few 90° and 0°/90° tests prior to complete failure, and determine absolutely that shear failure actually began within the reduced section, and not at the load transfer interface.

Some important features associated with kink bands are shown in Figure 9 for the 0° graphite/PEEK composite; similar observations were made for the 0° E-glass/epoxy. In Figure 9a, the tip of the lower edge of a kink progressing from right to left is imaged. The fibers are trapped in the flexed state, and a large number of them show evidence of fracture or their tensile sides (arrows). On the other hand, the tip of the kink band shown in Figure 9b is relaxed, as indicated by the perfectly straight fibers (arrow) adjacent to the last kinked segment. This suggests that the nucleation of the individual fiber fractures as the kink progresses is being accommodated by inelastic (reversible) deformation of the matrix.

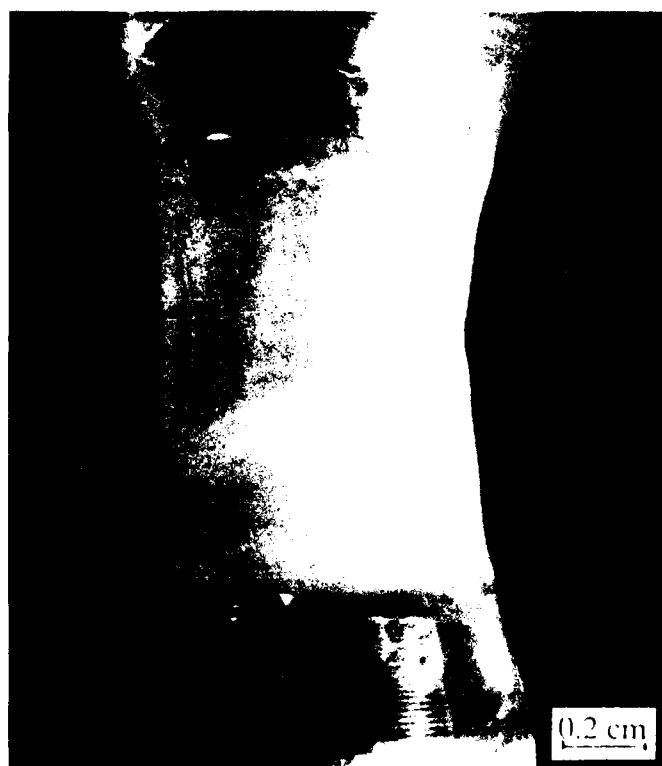
In the 0°/90° configuration, two types of microscale damage are observed, both confined to the 90° laminates. At low hydrostatic pressures, axial splitting occurs (Figure 10a); this is totally inhibited at pressures in excess of a few MPa. At all pressures, large numbers of microshear bands are nucleated throughout the 90° sectors, as shown in Figure 10a. The bands consist of crack



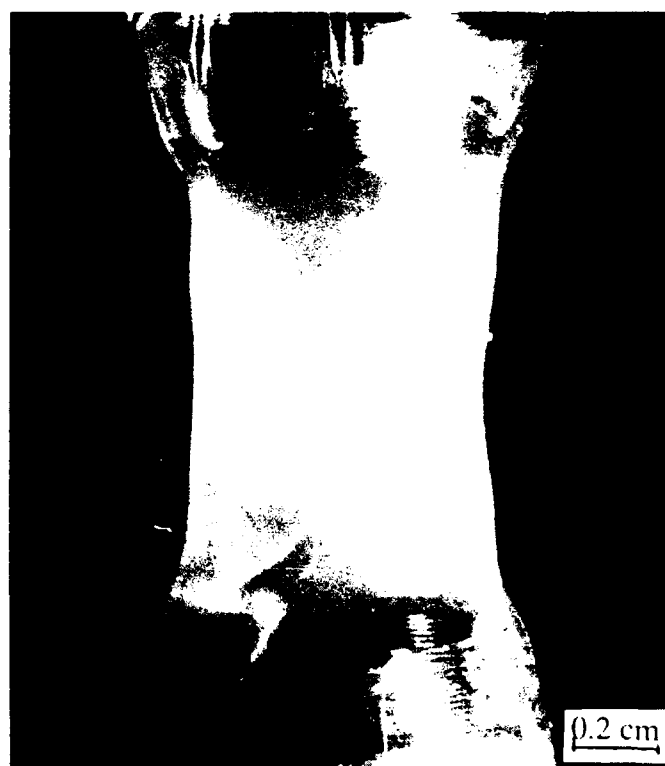
(b) 0° graphite/PEEK, $\sigma_1 = 50$ MPa



(a) 0°/90° E-glass/PEEK

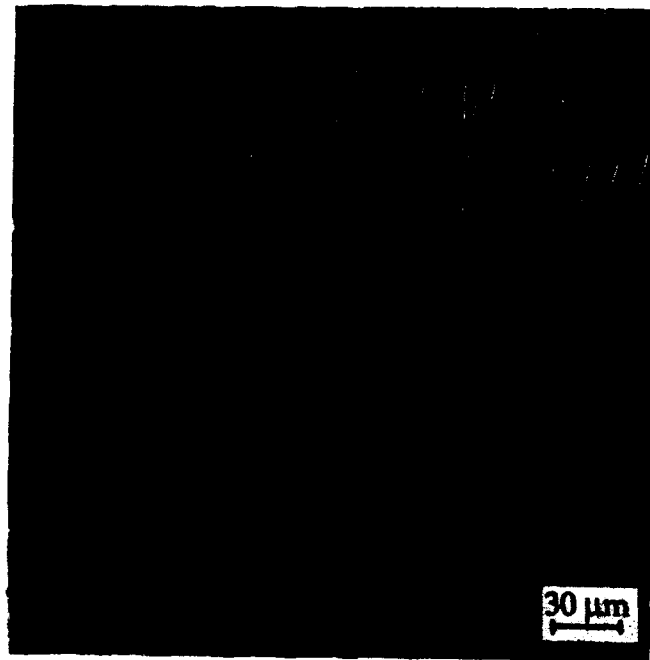


(c) 0° E-glass/epoxy, $\sigma_1 = 150$ MPa

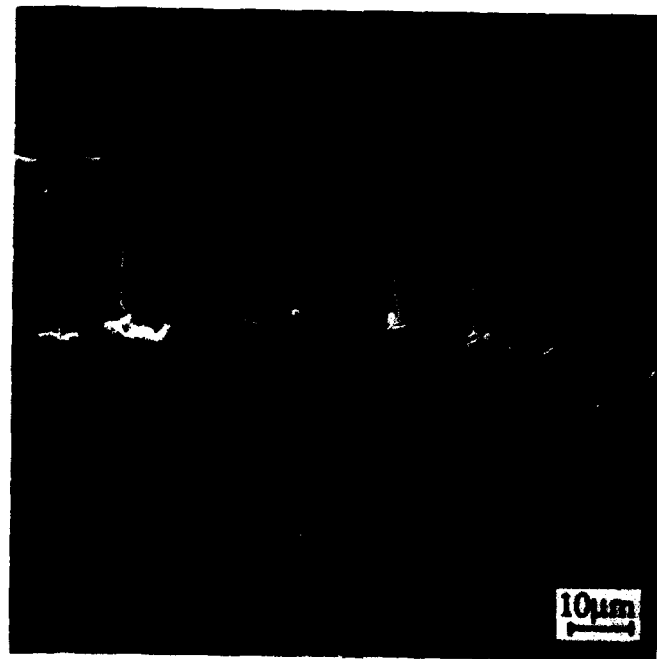


(d) 90° E-glass/epoxy, $\sigma_1 = 150$ MPa

FIGURE 8. Macroscopic composite failure modes.

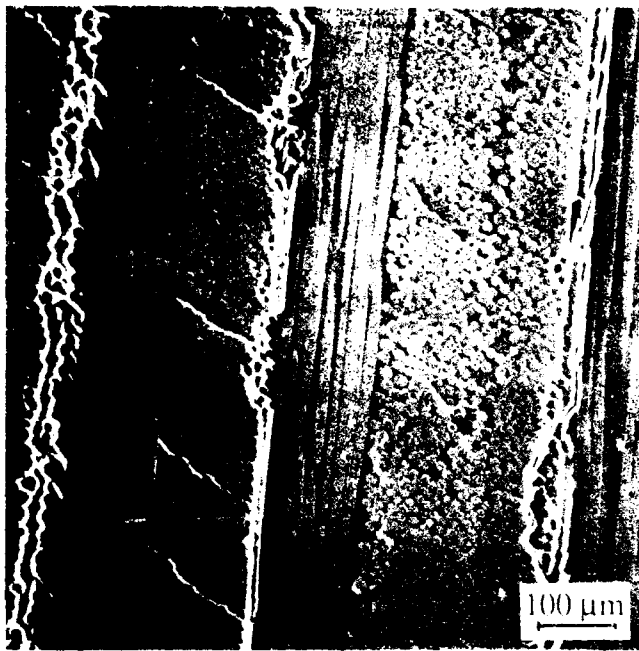


(a) Flexed kink tip, showing multi-fiber fracture (arrows) ahead of tip within inelastic or plastic zone.

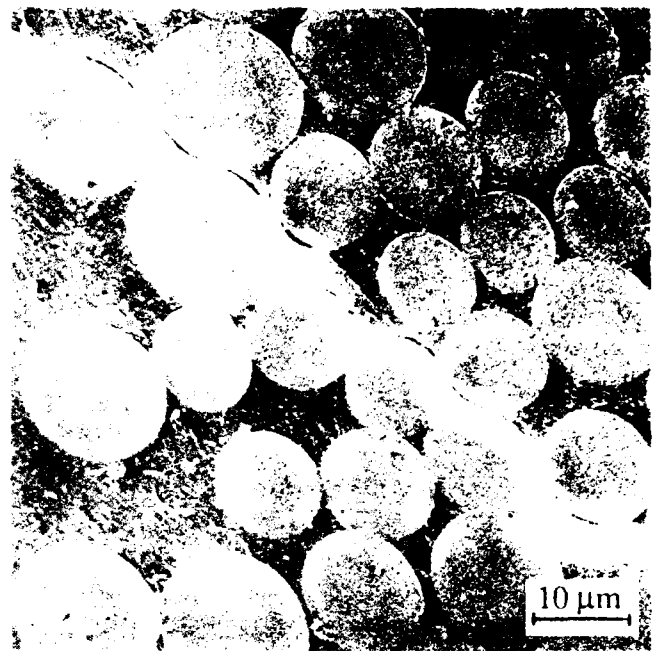


(b) Relaxed kink tip; flexure of kink deformation zone can be reversible (arrow).

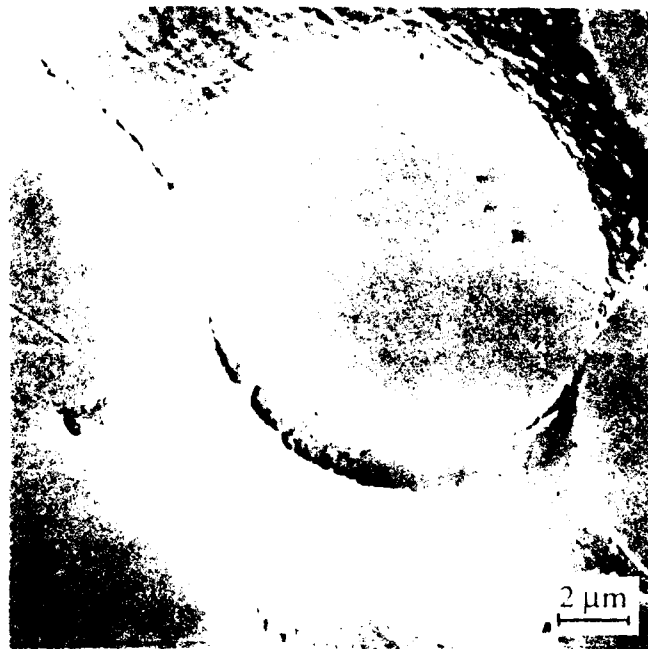
FIGURE 9. Kink details in 0° graphite/PEEK; $\sigma_3 = 0$, stress axis approximately vertical.



(a) Axial splitting and shear microfracture, both within 90° laminates.



(b) Details of isolated microshear band.



(c) Breakdown of fibrillar craze structure at fiber-matrix boundary.

FIGURE 10 Shear damage mechanisms in 0°/90° E-glass/PFEK; $\sigma_1 = 0$, stress axis vertical.

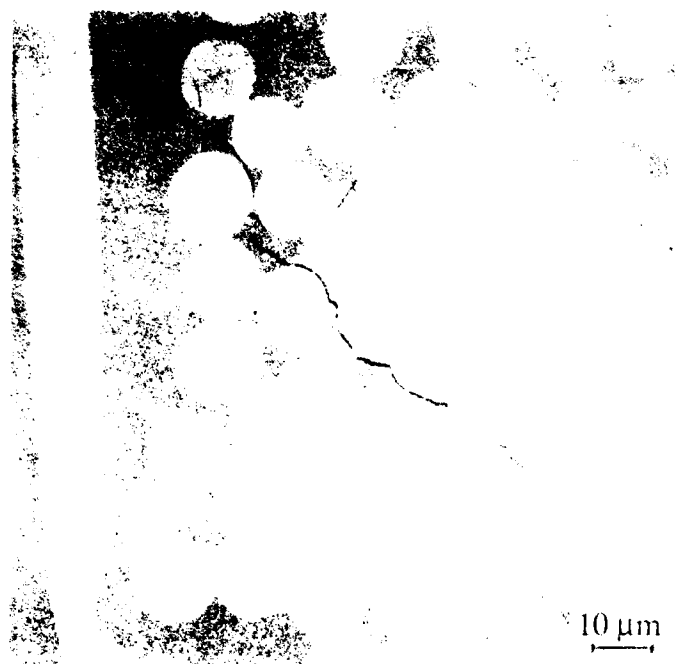
segments centered on 90° fibers (Figure 10b); the segments form by the breakdown of fibrillar craze structures nucleated at the fiber-matrix interface (Figure 10c). It is evident that the axial lay-ups constitute the ultimate barriers to the growth of the bands (Figure 10a), and that their failure must constitute the final link in the chain of events controlling the life of the specimen. At higher pressures, the 90° shear cracks occur at the same locations (fiber-matrix interface) and at about the same angle relative to the stress axis (Figure 11a). Despite the fact that the microcracks appear somewhat more tightly closed, they still form via craze dilatation and breakdown (Figure 11b), and their ultimate effect is indeed to cause certain 0° sectors to fail by micro-kinking (Figure 11c).

By comparison, simple 90° composites do not display the multiple microshear banding characteristic of 0°/90° lay-ups. Instead, failure appears to initiate at a single near-surface site in the form of a shear band which subsequently grows across the entire, otherwise undamaged, specimen (Figure 12).

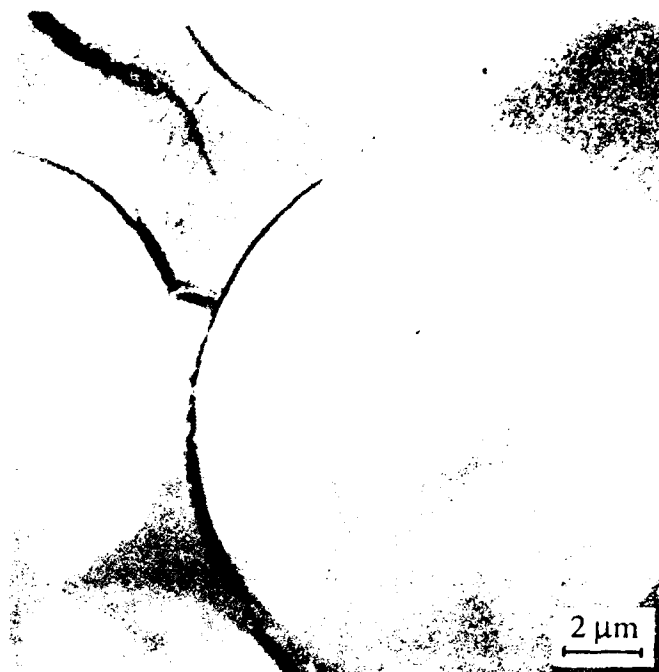
Discussion

Before dealing with the implications of these results, it is first necessary to rationalize their obvious variance with those obtained in nominally similar experiments by Weaver and Williams.¹³ In particular, for 0° PAN graphite-reinforced epoxy, the initial dependence of $\sigma_1 - \sigma_3$ upon confining pressure was found to have been rather robust, versus the mild pressure dependence obtained here for 0° PAN graphite-reinforced thermoplastic and E-glass-reinforced graphite. This difference is shown in Figure 13; it should be noted that above hydrostatic pressures of about 100 MPa, the results of Weaver and Williams¹³ and the present experiments follow similar pressure dependencies.

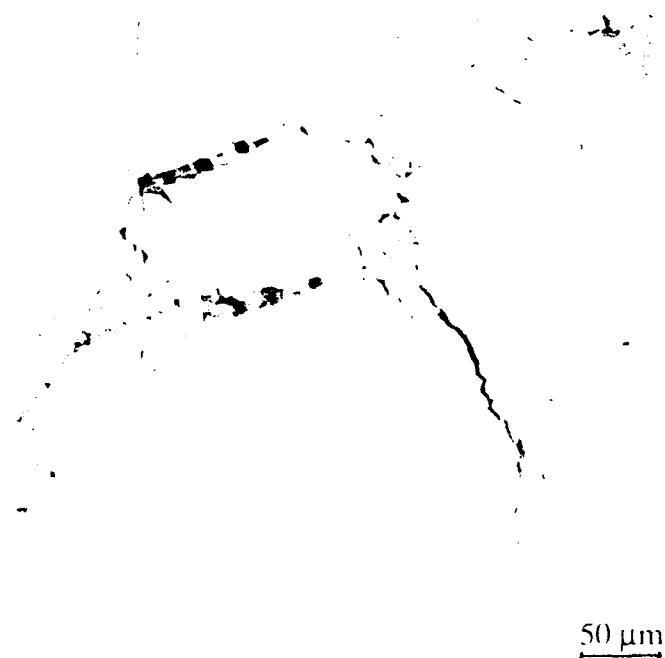
The early (pressure) functional difference almost certainly reflects the fact that specimen restraint was radically different in the two sets of experiments. Weaver and Williams used straight-sided right circular cylinders, with no reduced gage section, and more importantly, the ends of the samples were not provided with any radial support, other than positive confining



(a) Shear craze-cracks in 90° lay-up.



(b) Details of craze breakdown.



(c) Failure of 0° elements by 90° shear band cracks.

FIGURE 1. Shear damage development in 0°/90° E-glass/PEEK at $\sigma = 150$ MPa, stress axis vertical.

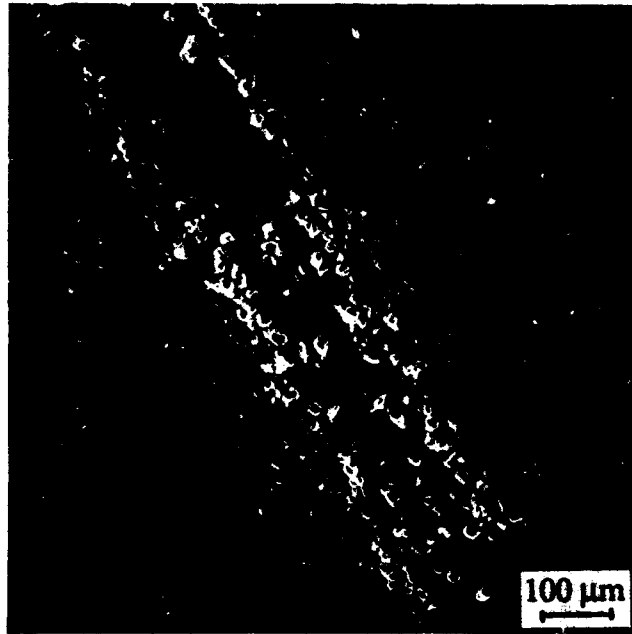


FIGURE 12. Shear failure in confined 90° E-glass/epoxy, showing absence of bulk damage otherwise; $\sigma_3 = 150$ MPa, stress axis vertical.

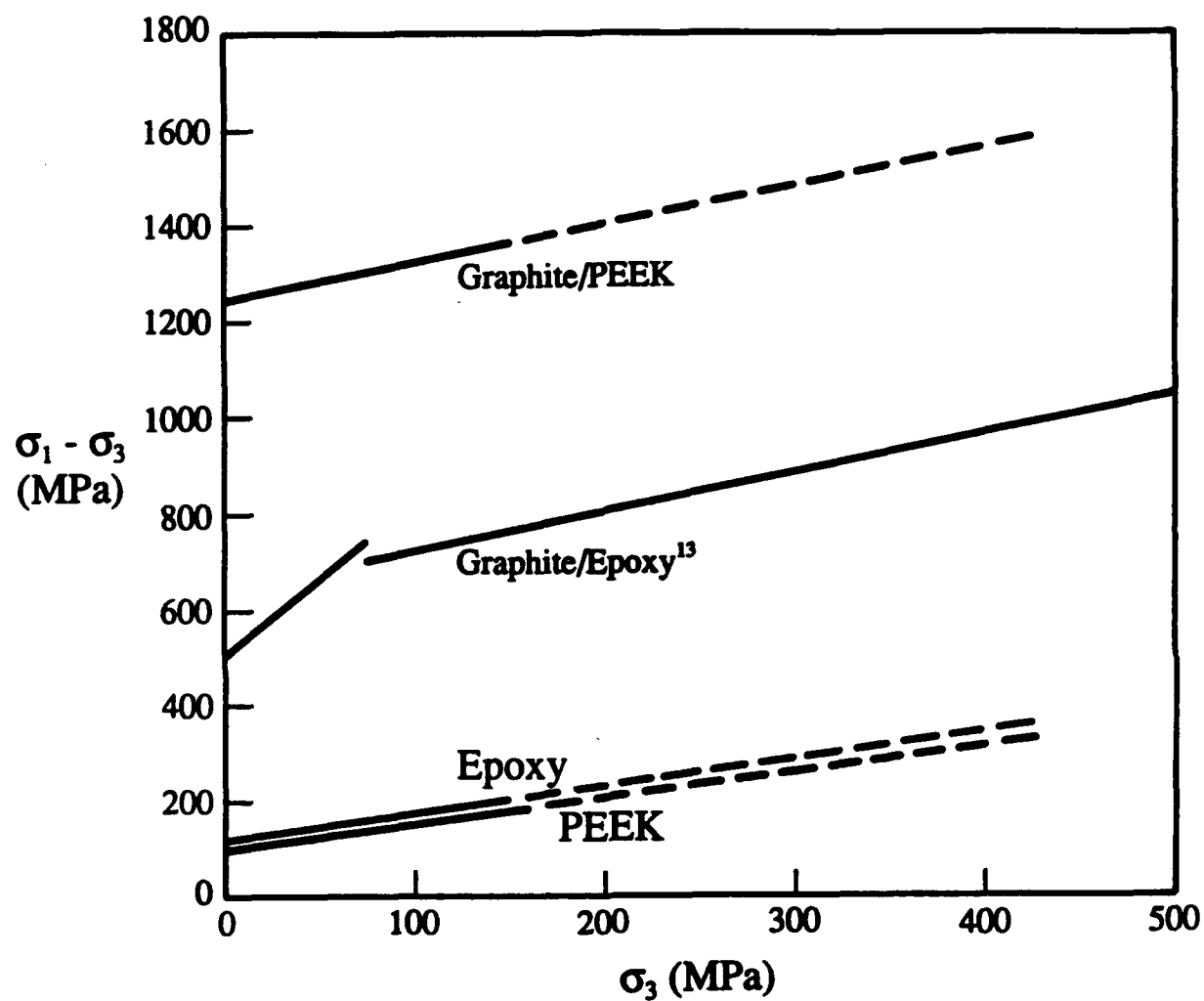


FIGURE 13. Pressure dependence of failure strength for uniaxially-reinforced graphite/PEEK and graphite/epoxy,¹³ compared with pressure dependence of flow stress for pure polymer matrices.

pressure, to prevent brooming and other transition failure modes from initiating at the specimen/platen interface. Thus, as shown photographically in their paper,¹³ there was a gradual transition, as the pressure rose from ambient to several hundred MPa, from brooming to local end splitting to platen-nucleated kinking to (finally) "true" kinking within the specimen gage section, where it remained during experiments at higher pressures. Because of the rings supporting the edges of the specimen ends in the present work, failure for all pressure conditions (and composite lay-ups) occurred within the gage section.

Thus, an initial conclusion is that the true pressure dependence for compressive failure of polymeric composites is mild, and in fact appears to reflect quite directly the pressure dependence measured for the flow stress of the matrix itself (Figure 13). That is, over a given pressure range, the increase in matrix flow stress is reasonably well in accord with the strength decrement affected in the corresponding composites as well, irrespective of lay-up or fiber type. This observation is especially evident for the 0° graphite/PEEK, 0°/90° E-glass/PEEK, and 90° E-glass/epoxy data.

That being the case, it appears that were it not for the matrix pressure sensitivity (in terms of either flow stress or pre-flow inelastic deformation, or both), the compressive strengths of the composite variants would be virtually independent of pressure. If the composites were homogeneous-isotropic, this would lead to the immediate conclusion that failure was totally shear dependent, and probably controlled by the maximum resolved shear stress $(\sigma_1 - \sigma_3)/2$, since the compressive strength represented a fixed value of $\sigma_1 - \sigma_3$, independent of pressure.

However, the composites are not isotropic-homogeneous, so that the maximum shear stress criterion does not apply. Instead, it must be recognized, as pointed out by Weaver and Williams,¹³ that the applied shear stress at failure is given by

$$\tau = (\sigma_1 - \sigma_3) \sin \theta \cos \theta \quad (1)$$

where θ is the angle between the plane of the local fracture which initiates the kink band and the direction of the maximum principal stress, *i.e.*, σ_1 . Unfortunately, knowledge of τ is indeterminate, since the angle θ refers to a local event those specifics are compromised by the inability to pinpoint its location, as well as the immediate buckling of associated fibers and the subsequent development of the mature kink band structure. As noted by others,^{12,13} the final orientation of the kink band *per se* is determined by minimum matrix plastic strain energy considerations associated with kink segment dimensions and fiber spacings, and is divorced from the pre-kink condition based on volumetric inelastic strain energy and the fiber flaw distribution that controls fibrous flexural strength.¹² Overriding these factors, that make it virtually impossible to quantify θ , hence τ , is the fact that some shear stress criterion governs failure for each composite.

Several factors combine to determine the precise value at which 0° lay-ups fail in compression. The flow stresses (and pressure dependent (in)elastic moduli) of the PEEK and epoxy resins are nearly equivalent, yet the compressive strengths of the graphite/PEEK and E-glass/epoxy are not. The difference apparently lies in the fiber reinforcement; in particular, the composite strength differential must derive from the relative severity of fiber flexure(s) in the initial lay-ups, or the relative fiber flaw distributions, or (most likely) these factors in combination.

It is interesting that there persists so little scatter in the graphite/PEEK strength-pressure relationship (Figure 5) versus that for the E-glass/epoxy composite. In the case of the former, it has been shown¹⁹ that fiber failure occurs by the nucleation of shear bands on the compressive sides of (PAN) graphite fibers, which in turn initiate tensile failure on opposite sides. This is not a flaw dominated process, but rather one which depends on a nominal material property, *i.e.*, the fiber shear strength. Hence, it should be very repeatable, and would be expected to produce little scatter in any failure mechanism that it controls. Earlier work has shown¹⁸ that this fiber shear mechanism is in fact operative within 0° graphite/PEEK composite kink bands produced by uniaxial compression (such as that shown in Figure 9).

The failure strength of E-glass fibers, on the other hand, is related solely to a surface flaw-dominated statistical strength distribution. Since failure occurs at sites of high misorientation, this produces significant variability in the "intrinsic" strength of the localized misoriented sector, with commensurate variability in the resulting composite strength. This probably is reflected in the apparent pressure-independent compressive strength of the 0° E-glass/epoxy composite shown in Figure 5. Over this limited pressure range, the scatter in the strength of individual composite samples due to fiber strength statistics within small, misorientation-activated failure zones was sufficient to hide the influence of matrix pressure-dependent strength on that of the composite.

The behavior of 0°/90° composites reflects directly the influence of pre-failure shear within the 90° laminates. Strength is lower than that of pure axial lay-ups because 0° sectors are being "attacked" by large shear microcracks, rather than small initial misorientations in axial fibers. The pressure dependence is similar to that of PEEK alone, reflecting both intrinsic matrix dilatation, as well as the extra dilatation required to open up craze-induced shear microcracks.

IV. CONCLUSIONS

Some important conclusions can be drawn from the foregoing. First, the mild pressure sensitivity of the compressive failure dependence of fiber-reinforced polymeric composites indicates that the failure mechanism is shear dominated, *i.e.*, dilatational factors are insignificant. Since it appears that failure may initiate at sites of inelastic (but nevertheless large strain) deformation, it may be insufficient to focus on higher yield or flow stress as a route to enhanced composite performance. In particular, the in(elastic) modulus may be at least as relevant. Since matrix deformation and the vagaries of fiber misorientation determine the exact site of compressive failure initiation, intrinsic fiber strength (average strength versus Weibull modulus) is more important than is the case for tensile situations.

V. ACKNOWLEDGEMENTS

The support of the Office of Naval Research under Contract N00014-92-C-0093 is gratefully acknowledged. Careful experimental work by, and helpful discussions with, A. Nicholls are greatly appreciated.

VI. REFERENCES

1. S. R. Frost, *J. Compos. Mater.*, **26** (1992) 1151.
2. S. R. Swanson, *Trans. ASME* **114** (1992) 8.
3. D. C. Lagoudas, I. Tadjbakhsh, and N. Fares, *J. App. Mech.* **58** (1991) 473.
4. M. R. Wisnom, *Composites*, **21** (1990) 403.
5. S. L. Bazhenov and V. V. Kozey, *J. Mater Sci.*, **26** (1991) 6764.
6. H. T. Hahn and J. G. Williams, *Composite Materials: Testing and Design*, ASTM STP 893, ed. J. M. Whitney, American Society for Testing and Materials, Philadelphia (1986) 115.
7. H. F. Wu and J. R. Yeh, *J. Mater. Sci.*, **27** (1992) 755.
8. H. T. Hahn, ICCM⁶ & ECCM², Vol. 1, ed. F. L. Matthews, N. C. R. Buskell, J. M. Hodgkinson, and J. Morton, Elsevier, NY.
9. R. J. Lee, "Compression Strength of Aligned Carbon fiber-Reinforced Thermoplastic Laminates," *Composites*, **18** (1), (1987) 35-39.
10. D. Purslow, "Fractography of Fiber-Reinforced Thermoplastics, Parts 3. Tensile, Compressive, and Flexural Failures," *Composites*, **19** (5) (1988) 358-366.

11. B.W. Rosen, "Mechanics of Composite Strengthening," *Fiber Composite Materials*, (1965) 37.
12. A. G. Evans and W. F. Adler, *Acta Metall.*, **26** (1978) 725.
13. C. W. Weaver and J. G. Williams, *J. Mater. Sci.*, **10** (1975) 1323.
14. I. M. Ward, *J. Mater. Sci.*, **6** (1971) 1397.
15. W. A. Spitzig and O. Richmond, *Poly. Eng. Sci.*, **19** (1979) 1129.
16. J. A. Sauer, *Poly. Eng. Sci.*, **17** (1977) 150.
17. J. Lankford, *Ceramic Eng. Sci. Proc.* (submitted).
18. J. Lankford, "Compressive Damage and Failure at High Loading Rate in Graphite Fiber-Reinforced Polymeric Matrix Composites," *Advanced Composite Materials*, ed. M. D. Sacks, American Ceramic Society, Westerville, OH, (1991) 553-563.
19. M. G. Dobb, D. J. Johnson, and C. R. Park, *J. Mater. Sci.*, **25** (1990) 829.

II.

FAILURE MECHANISMS IN A UNIDIRECTIONAL FIBER-REINFORCED THERMOPLASTIC COMPOSITE UNDER UNIAXIAL, IN-PLANE BIAXIAL, AND HYDROSTATICALLY CONFINED COMPRESSION

by

H. Couque,^{*} C. Albertini,^{} and J. Lankford^{*}**

^{*} Southwest Research Institute

San Antonio, TX 78228

^{} Commission of the European Communities Joint Research Center
Ispra, Italy**

ABSTRACT

The deformation and damage of a unidirectional carbon fiber-reinforced composite was characterized under hydrostatically confined uniaxial and in-plane biaxial compression. The failure process under uniaxial loading was observed to involve kink bands combining into a macroscopic shear band. Incidental interlamellar splitting was observed, its extent decreasing with hydrostatic pressure. The composite was found to exhibit markedly lower in-plane biaxial failure strength in the direction parallel to the fibers when compared to the uniaxial case. It is shown that the origin of the six-fold strength differential between the two situations probably lies in the involvement, via state-of-stress, of two different, specific manifestations of fiber lay-up imperfection.

I. INTRODUCTION

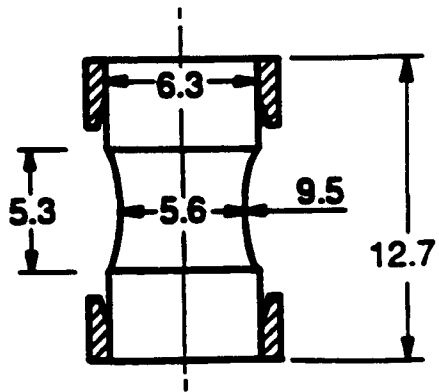
Certain practical situations require that fiber-reinforced polymeric matrix composites be able to withstand compressive loadings parallel to the fiber direction. Recent investigations have been conducted to establish the onset of initial instability in polymeric-matrix composites subject to simple uniaxial loading.¹⁻³ Transferability of these results to more complex mixed-mode compressive loading situations remains to be demonstrated. The objective of the present paper is to report on the characterization of strength and damage mechanisms for a unidirectional carbon fiber-reinforced composite subject to compressive loading under hydrostatically-confined uniaxial loading versus in-plane biaxial loading at nominally equivalent off-axis maximum stress levels.

II. EXPERIMENTAL PROCEDURES

Materials

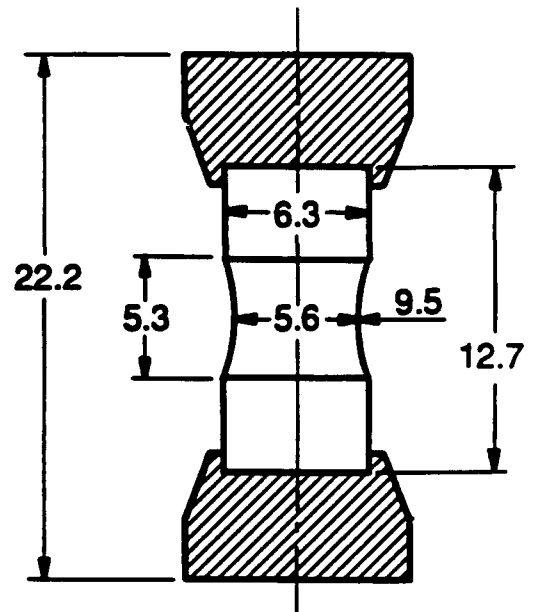
The material selected for study was a polyetheretherketone (PEEK) matrix, polyacrylonitrile (PAN)-derived carbon fiber-reinforced composite. The matrix is a semicrystalline thermoplastic of approximately 23,000 molecular weight, whose properties and microstructure are extremely sensitive to thermal history. In producing the present composite, the matrix was melt impregnated at 380°C for 30 minutes; subsequent heat treatment resulted in a spherulitic microstructure revealed by argon ion etching to be on the order of 8 μm in size.

Carbon fibers (Type AS4) approximately 7 μm in diameter were laid up unidirectionally, with a nominal 60% fiber density. There was a significant waviness to the fibers, *i.e.*, uniaxial alignment was by no means perfect, and although the void density was under 1%, the voids which were present tended to cluster. Both of these defects are typical of carbon fiber/PEEK composites.

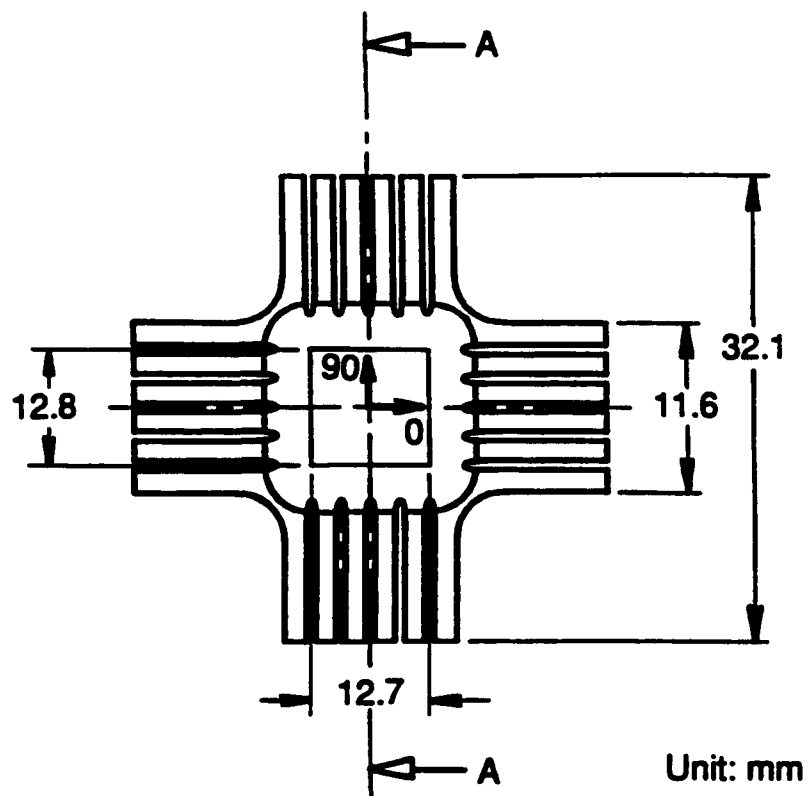
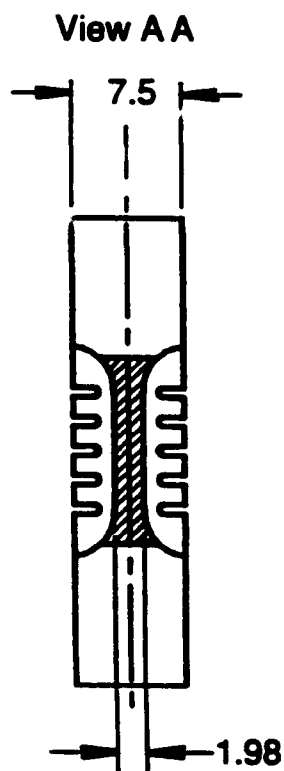


Unit: mm

(a) Uniaxial



(b) Confined pressure



Unit: mm

(c) Biaxial

FIGURE 1. Compression specimen configurations.

Experimental Approach

Compression testing was conducted under uniaxial and biaxial loading conditions at a strain rate of about 10^{-4}s^{-1} . The specimen arrangement, shown in Figure 1a and 1b, minimized gripping and end effects and favors failure within the gage section.¹ The material is shaped into a cylinder, 6.3 mm in diameter by 12.6 mm in length, with a reduced gage section 5.6 mm in diameter. For conventional uniaxial compression testing, the specimen (Figure 1a) was reinforced with internally chamfered rings around the bases made of high-strength steel, honed to a snug fit. A similar configuration was used for uniaxial testing under confined pressure, with the difference that the chamfered rings were a part of the loading platens (Figure 1b). This configuration permitted the application of a uniform confining pressure to the gage section. All specimens, as well as the matching hardened steel load platens, were carefully machined so that the mating surfaces were parallel within $4\text{ }\mu\text{m}$ over the entire load surface. These uniaxial tests were performed under crosshead control in a servo-controlled hydraulic machine.

Uniaxial tests under confined pressure were conducted using a pressure vessel filled with di-2-ethyl hexyl sebacate pressure transmitting fluid at a pressure varying from 50 to 250 MPa.⁴ The hydraulic ram applied axial loading through sliding O-ring seals and a bridge of four electrical resistance strain gages inside the pressure vessel measured the axial load. Hydrostatic pressure produced a zero shift in the output of this load cell, the magnitude of which was measured and subtracted from the load measurements. Hydrostatic pressure was measured by a diaphragm-type electrical pressure transducer located at the fluid inlet orifice of the pressure vessel.

Biaxial testing was conducted using a unique electromechanical biaxial testing device⁵ employing a biaxial cruciform specimen, shown in Figure 1c. The specimen has a uniform gage section $12 \times 12\text{ mm}$ in area and 1.9 mm in thickness. Loading was accomplished in the fiber

* Ispra, Italy

direction (0°) and normal to it (90°) with a set of bars 17.5 mm in diameter made of high-strength steel. The load was monitored using strain gages located on the bars, while strain in the gage section was measured by means of a 45° rosette strain gage.

In order to establish the microstructural damage basis for the compressive behavior of the specimens, they were sectioned, polished, and examined by optical microscopy. Prior to sectioning, samples were mounted in epoxy to preserve the damage features during preparation.

III. RESULTS

Strength and failure strain characteristics of the composite in the 0° direction are shown in Figure 2a and Table I. Under uniaxial loading conditions, at confining pressures ranging from ambient to 150 MPa, the composite exhibits comparable failure properties. Increasing the hydrostatic pressure to 250 MPa, a stiffer response along with a slight increase in ultimate strength is observed. A quite different response is reached with the biaxial specimen, the early response of which follows a path similar to that of the uniaxial specimen tested at a confining pressure of 250 MPa. At a small strain, on the order of only 0.0015, the capacity to carry load decreases, resulting in premature (versus the uniaxial case) failure. In particular, the failure strain is lower by more than 75%, when compared to uniaxial failure strains. This is reflected in a dramatic, six-fold decrease in the axial failure stress.

The deformation response of the biaxial specimen within the two loading directions, 0° and 90° , is shown in Figure 3. Large strains are reached in the direction perpendicular to the fibers. In this orientation, the failure strain is about twice that reached in the 0° direction for the pure uniaxial case (Table I and Figure 3).

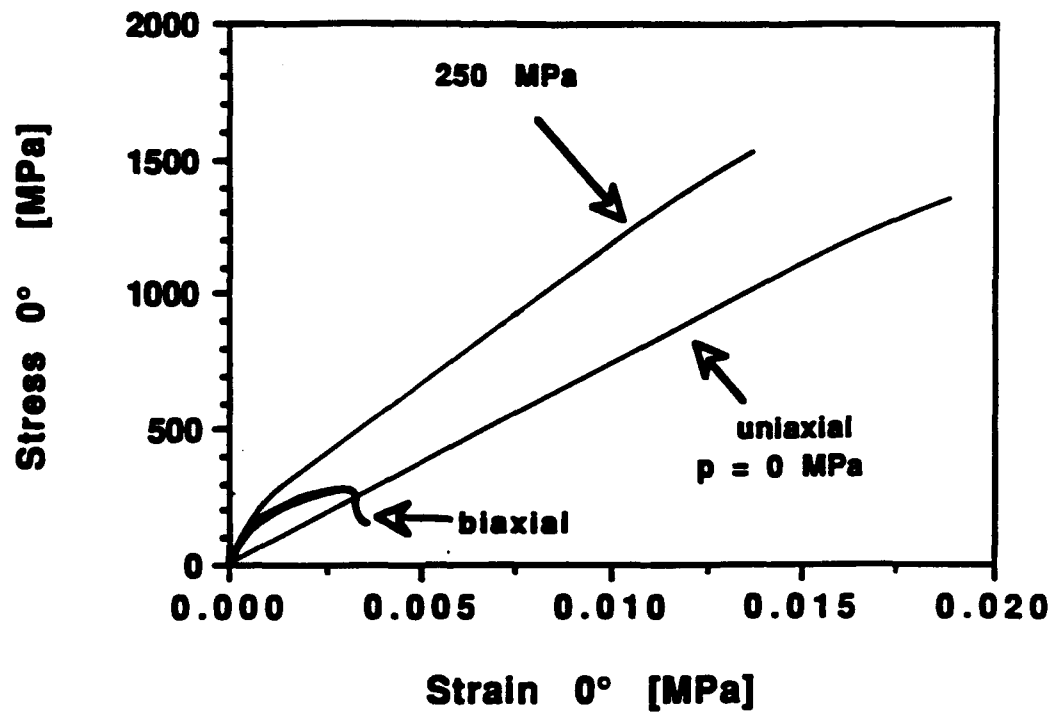


FIGURE 2. Engineering stress-strain response in the fiber direction for uniaxial and biaxial experiments.

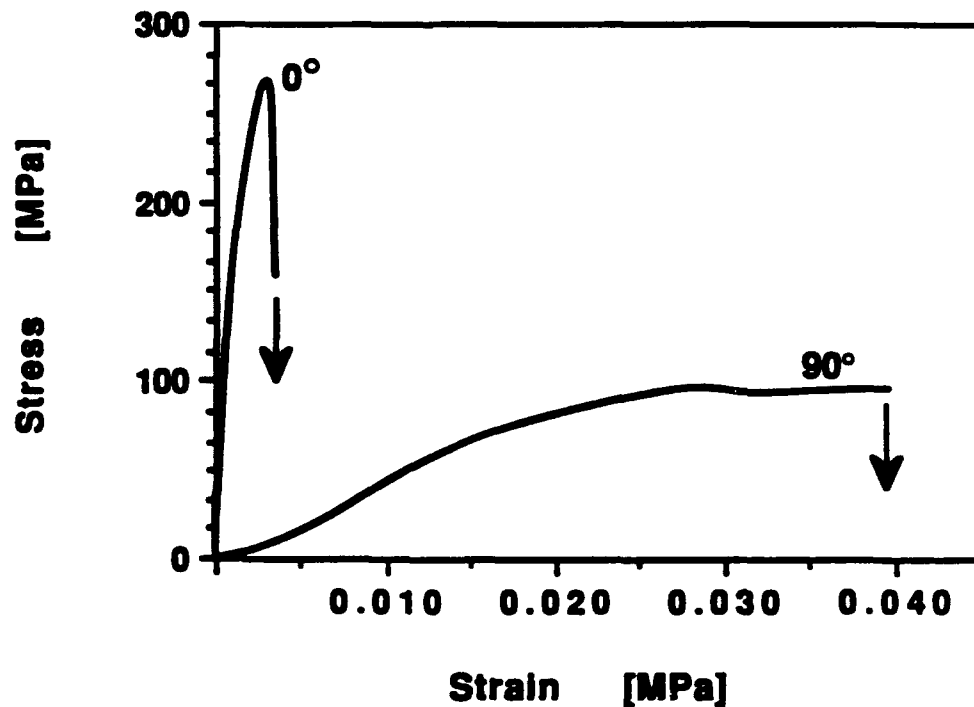


FIGURE 3. Engineering stress-strain response in the two loading directions for the biaxial experiment.

TABLE I
RESULTS OF THE COMPRESSION TESTS

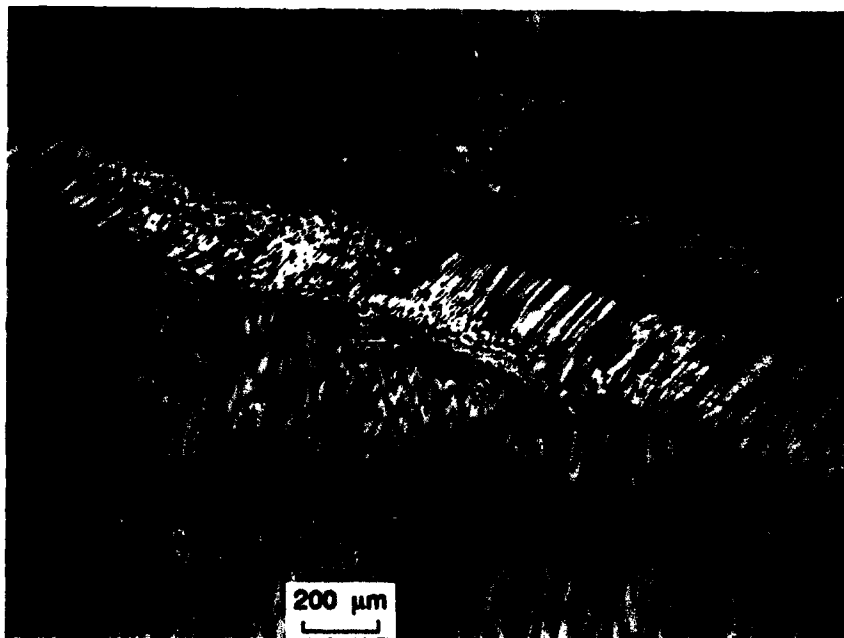
Loading Direction	Hydrostatic Pressure (MPa)	Compressive Strength (MPa)	Failure Strain
Uniaxial 0°	0	1390	0.019
Uniaxial 0°	150	1370	0.018
Uniaxial 0°	250	1540	0.014
Uniaxial 0°	0	167	0.003
Uniaxial 90°	0	97.0	0.031

Characterization of Damage Mechanisms and Discussion

Figure 4a shows a macroscopic section of a uniaxial specimen tested under the highest confining pressure, 250 MPa, where a shear band oriented at about 75° from the load axis is observed. A higher magnification view of the shear band reveals it to be composed of multiple kink bands (Figure 4b). At ambient pressure, similar features are observed, as shown in Figure 5, but in addition interlamellar fractures are present. This indicates that shear banding deformation under reduced lateral constraint favors tensile interlamellar fracture. However, it has been shown elsewhere⁶ that this damage mode is an incidental effect of the shear displacement associated with breakdown of the shear kink band. Axial splitting is not the basis for the ambient versus 250 MPa pressure strength differential, which instead is a reflection of the pressure sensitivity of the thermo-plastic matrix. It is the latter which stabilizes the 0° fibers against the nucleation of an initial microkink at the site of highest (local) fiber misorientation. The surrounding, more axially oriented fibers tolerate high stress levels until the small volume containing the misoriented fiber(s) is activated.



(a) Full section

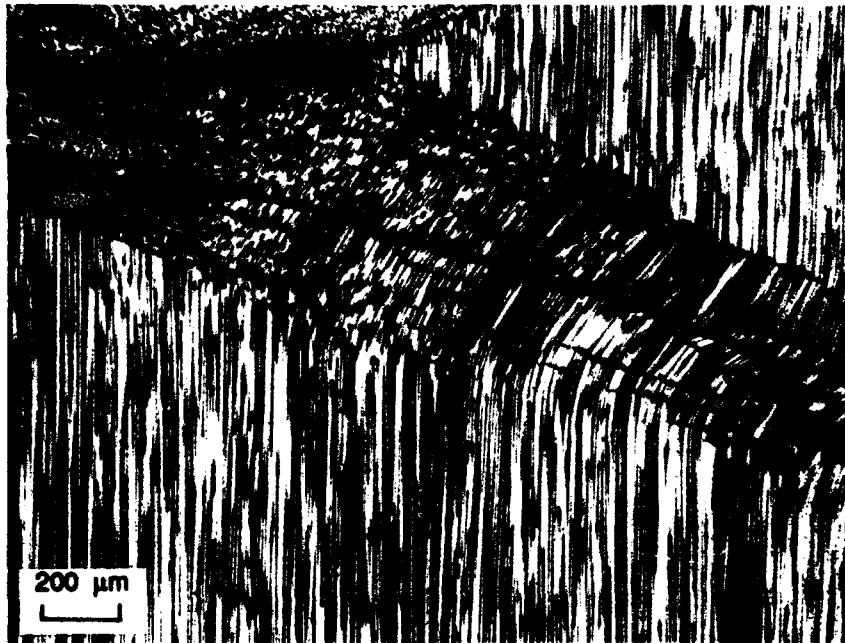


(b) Detail of the shear band fracture.

FIGURE 4. Section of uniaxial specimen tested at a confining pressure of 250 MPa.



(a) Full section



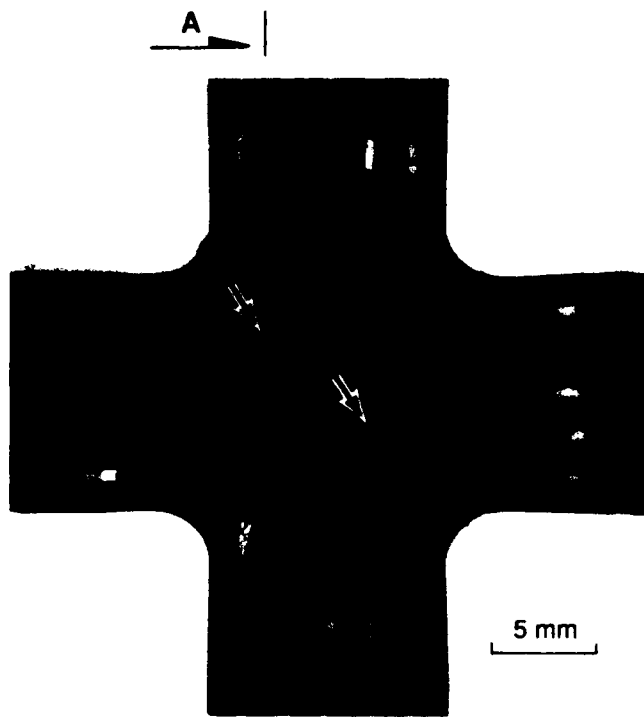
(b) Detail of the shear band fracture

FIGURE 5. Section of uniaxial specimen tested under ambient pressure.

In the case of the biaxial failure, on the other hand, the situation is somewhat different. As shown in Figure 6a, the failure process of this specimen involves localized bands (arrows) parallel to the 90° loading direction. A section of one of these (Section AA) is shown in Figure 6b. This section shows that failure involved macroscale buckling within the gage section, buckling which was more or less symmetric about the midplane. At higher magnification (Figure 6c), it can be seen that near the outer fiber of the sample, fiber flexure in the unfailed lower right hand sector was intense, but continuous. However, near the interior, fiber fracture has already occurred, nucleating several kink bands (arrows) which are in the process of moving from the interior to the surface. The latter stages of this process can be seen in the lower left hand kink array, where the kink segments are misoriented by more than 90° in the interior (arrow A), but much less so near the surface (arrow B). Again, an interior kink nucleation event seems to have occurred.

Clearly the shear splitting took place as an aftermath of the mature kink band development, and probably constituted the failure event which terminated the region of stable load drop. The axial splitting is even less consequential, deriving simply from the wedging action of the blunt "knife" created by the catastrophic shear band fractures, which probably are also responsible for the post-failure nucleation of exterior kink bands such as those indicated by arrow C.

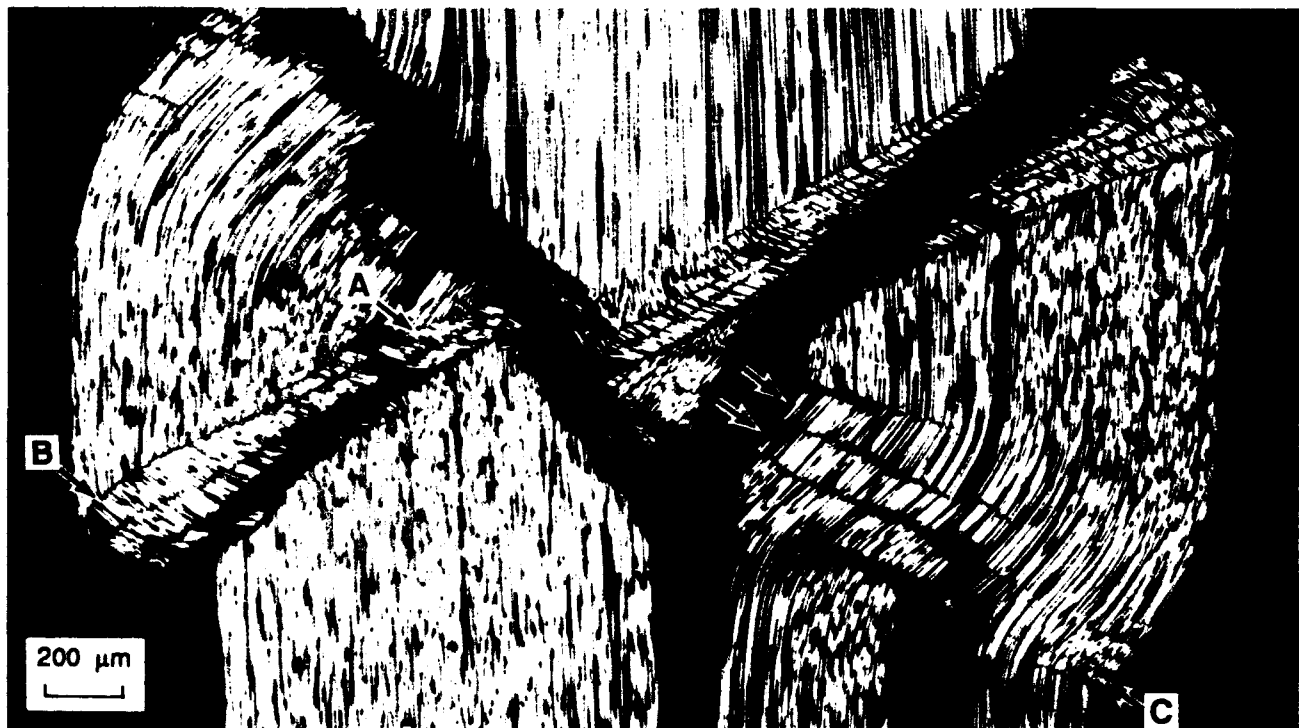
The most reasonable basis for low stress buckling failure during biaxial compression lies in two synergistic factors: out of plane compliance, and the natural waviness of the fibrous lay-up. Here one does not mean highly local misalignment, such as that alluded to above as responsible for high-strength kinking, but instead the general, volumetric waviness of a group of long fibers. In particular, there is a certain probability that somewhere in the gage section, a number of fibers will share the same wave pattern, *i.e.*, they will be predisposed to buckle out of plane (the so-called shear mode), and to do so at much lower an overall stress level than that required to nucleate an axial kink. Once such an event begins to occur with rising load, the stress in the opposite side of the gage section will rise, and produce an unrestrained gage tendency toward buckling (outward bulging) on that side. A structural instability has now been set up, progressing as shown in



(a) Out of plane view of biaxial specimen, showing two deformation bands of 1 mm width normal to the fiber direction



(b) Photomicrograph of the sectioned specimen (Section AA)



(c) Details of kink/fracture zone in (b).

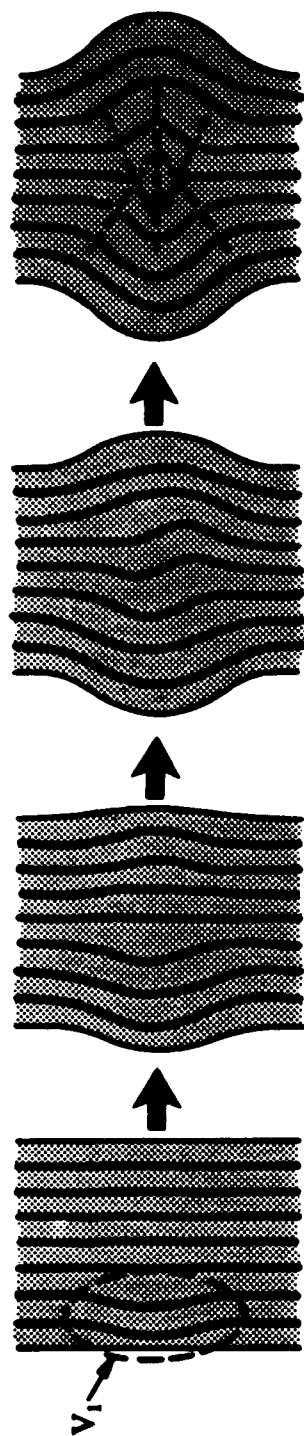
FIGURE 6. Biaxial damage development.

Figure 7a, versus the more localized series of events attending a high stress kink (Figure 7b). It will be noted that based on bend radii, it would be anticipated that final failure will occur by the initiation of sets of internal kink bands, as observed in Figure 6.

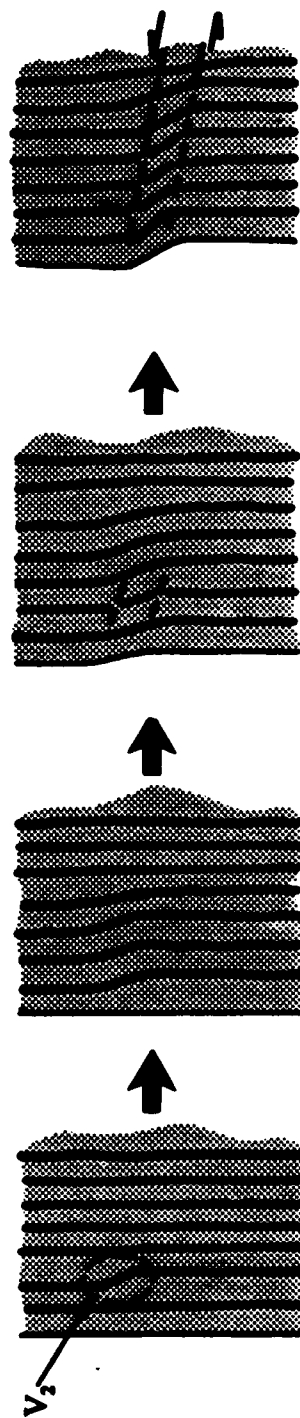
The situation just outlined for the biaxial case is a derivative of its essential stress asymmetry. For the cylindrical gage section, whether confined or unrestrained, the matrix is constantly expanding radially, so that regions adjacent to potential buckle sites basically move away from them, dampening their effect by denying the volumetric inflow of material required to "feed" the instability. Access to this mechanism through off-axis stress anisotropy is an effective deterrent to the attainment of the intrinsically greater ultimate strength represented by the kinking of individually misaligned fibers.

IV. REFERENCES

1. J. Lankford, "Compressive Damage and Failure at High Loading Rate in Graphite Fiber-Reinforced Polymeric Matrix Composites," *Advanced Composite Materials*, ed. M. D. Sacks, American Ceramic Society, Westerville, OH, 553, 1991.
2. A. G. Evans and W. F. Evans, *Acta Metallurgica*, **26** (1978) 725.
3. M. G. Dobbs, D. G. Johnson, and C. R. Park, *Journal of Materials Science*, **26** (1990) 829.
4. R. Arrowood and J. Lankford, *Journal of Materials Science*, **22** (1987) 3737.
5. C. Albertini, E. Blery Blionas, M. Micunovic, M. Montagnani, and E. V. Pizzinato, *Institute Physic Conferences Series*, No. 102 (1989) 173.
6. J. Lankford, *Journal of Materials Science* (submitted).



(a) Biaxial sequence; V_1 is volume associated with near surface fibers preferentially aligned for shear mode of microbuckling.



(b) Hydrostatic sequence; V_2 is volume associated with misaligned fiber segment.

FIGURE 7. Schematic of compressive sequence; $V_1 \gg V_2$.

III.

**THE EFFECT OF HYDROSTATIC PRESSURE
AND LOADING RATE ON COMPRESSIVE FAILURE
OF FIBER-REINFORCED CERAMIC MATRIX COMPOSITES**

J. Lankford

**Materials and Mechanics Department
Southwest Research Institute
6220 Culebra Road
San Antonio, Texas 78238-5166**

ABSTRACT

The influence of hydrostatic confinement on compressive strength and corresponding failure mechanisms is explored for SiC reinforced glass ceramics tested at different strain rates. Two composite architectures (0° and $0^\circ/90^\circ$) are studied, versus monolithic glass ceramic tested under similar conditions. Composite confined pressure results are interpreted in terms of fiber buckling under quasistatic conditions and fiber kinking at high pressures, and compared with monolithic (noncomposite) microfracture coalescence at low pressures versus shear band formation under more intense confinement.

I. INTRODUCTION

A number of studies¹⁻⁴ have shown that for purely monolithic (unreinforced) brittle materials, dilatational damage dominates the failure process, as manifested in significant increases in compressive strength with confining pressure. This dependence arises from the closure of grain-sized (or less) axial microcracks, which ultimately coalesce to cause failure. On the other hand, other recent experiments⁵ indicate that for polymeric matrix 0° and 0°/90° fiber-reinforced composites, compressive strength is relatively independent of hydrostatic pressure. This was interpreted in terms of shear dominance in the failure process.

The failure of fiber-reinforced ceramic matrix composites under even simple compression has been shown^{6,7} to be complex, so that it is not evident at present which of dilatation or shear actually controls failure. Both damage modes are, in fact, observed in combination with one another. Confined compression experiments, however, provide a seeming ideal vehicle for making this assessment, as has been the case for monolithic ceramics and polymeric matrix composites. As shown in Figure 1, the expansion of a cylindrical specimen due to an axial stress σ_1 is counteracted by the radial stress σ_3 . Moreover, the shear stress in the cylinder, for given values of σ_1 and σ_3 , is

$$\tau = (\sigma_1 - \sigma_3) \sin \theta \cos \theta \quad (1)$$

where $\sigma_1 - \sigma_3$ is the compressive stress within the material relative to the hydrostat, and θ is the angle which the plane of initial failure makes with the direction of σ_1 . If σ_1 represents the flow or failure stress for various values of σ_3 , the relative influence of shear versus dilatation can be determined by plotting $\sigma_1 - \sigma_3$ versus σ_3 . To the extent that relatively small changes in σ_3 create large increases in $\sigma_1 - \sigma_3$, dilatational crack initiation and/or growth mechanisms probably are involved. Conversely, the absence of pressure sensitivity in $\sigma_1 - \sigma_3$ (*i.e.*, a horizontal plot) would indicate that the strength (flow or failure) is controlled solely by a critical shear stress criterion. For a composite, this critical value is not necessarily⁸ the maximum macroscopic shear stress, as is

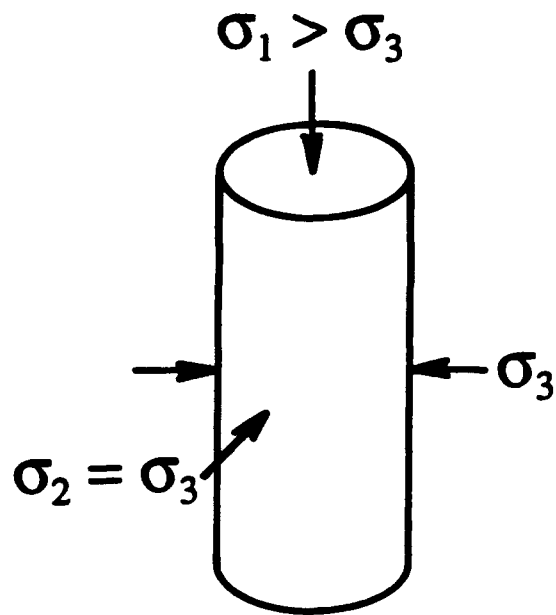


FIGURE 1. Schematic of stress distribution related to combined hydrostatic pressure–compression testing.

generally found to be the case for isotropic, homogeneous materials, but may relate to a certain angle of bend in the reinforcing fibers required to fracture them in local tension, and thereby produce a propagating kink band.

In the present paper, pyroceramic matrix composites with varying fiber architectures are subjected to combined compression and hydrostatic pressure. Similar experiments have been performed for unreinforced material similar to the composite matrix. Results are evaluated in terms of their implications regarding the relative roles of shear and dilatation in the micro-mechanics of failure.

II. EXPERIMENTAL APPROACH

Materials

The composites studied were composed of SiC fiber*-reinforced lithium-alumino-silicate (LAS), provided by United Technologies Research Center. Uniaxially reinforced material was tested in the ceramed condition. In addition, a cross-plyed (0°/90°) variant was studied, in this case the matrix being unceramed. The latter composite microstructure is shown schematically in Figure 2; both lay-ups contained about 46 vol. % fiber.

Unreinforced matrix was represented by a pyroceramic** similar in chemistry to the LAS matrix of the composite. The material was tested in the ceramed state, and as for the ceramed 0° composite, grain sizes were in the range 0.5 - 2.0 μm .

* Nicalon

** 9606, Corning Glass

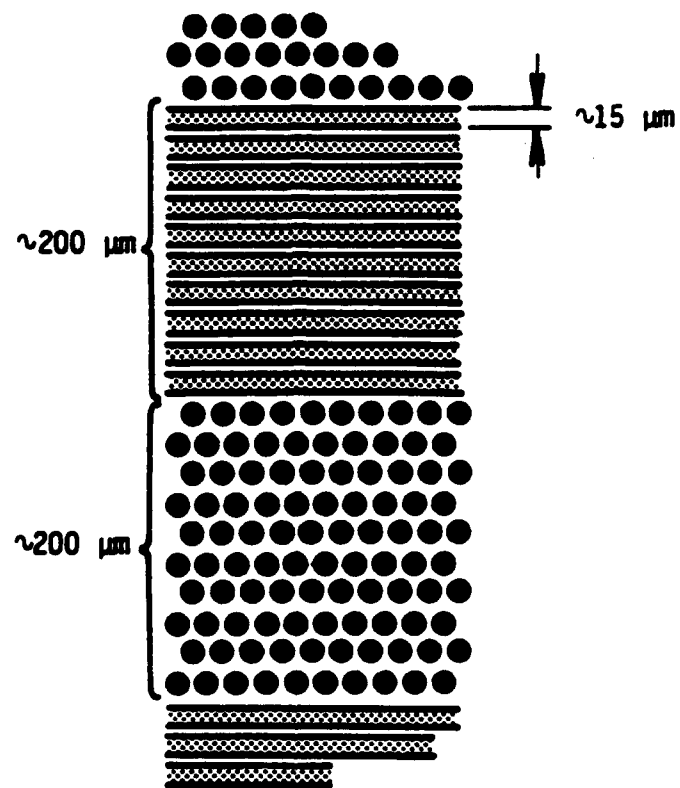


FIGURE 2. Dimensions and orientations of cross-ply bundles and fibers.

Specimen Design

Cylindrical specimens 1.2 cm long x 0.6 cm diameter were machined from sample blanks, and their ends were ground parallel to within 2 μm tolerance. The compression test axis was parallel to the fibers for the 0° samples, while for the 0°/90° material, the load axis was oriented parallel to the 0° direction.

To prevent brooming of the composites, and ensure valid gage section failure, their ends were constrained using caps of high-strength steel, precision honed to just slip over each specimen. Transition between the specimen and the load ram was provided by a conical shaped alumina platen; the entire load train is shown in Figure 3. Testing of the unreinforced matrix was similar, but in this case, the end caps were not required. To prevent the silicone-based pressure fluid from infiltrating surface pores and causing premature failure during confined pressure testing, samples were sealed within thin, heat-shrinkable Teflon tubing, overlapping the ends of the platens.

Test Procedures

Controlled strain rate tests were performed at approximately 10^{-4}s^{-1} and 1s^{-1} , with a servo-controlled hydraulic ram supplying the axial load. For tests with radial confining pressure, a special pressure vessel was utilized. In performing these experiments, the hydrostatic pressure was first raised to the desired level by pumping fluid into the pressure vessel while a servo-controller matched the axial stress to the pressure. The axial load was then increased under displacement control at fixed pressure. A bridge of four electrical resistance strain gages inside the pressure vessel measured the axial load. Since the hydrostatic pressure produced a zero shift in the output of this load cell, the magnitude of the shift was measured in a series of calibration runs and subtracted from the load measurements. Hydrostatic pressure was measured by a diaphragm-type electrical pressure transducer located at the fluid inlet orifice of the pressure vessel. The exact value of the strain rate, $\dot{\epsilon}$, was determined by measuring the stress rate, $\dot{\sigma}$, and calculating $\dot{\epsilon}$ using the appropriate value for Young's modulus, E , for each material, *i.e.*, $\dot{\epsilon} = \dot{\sigma}/E$. All samples were tested at room temperature, under confining pressures as high as 350 MPa.

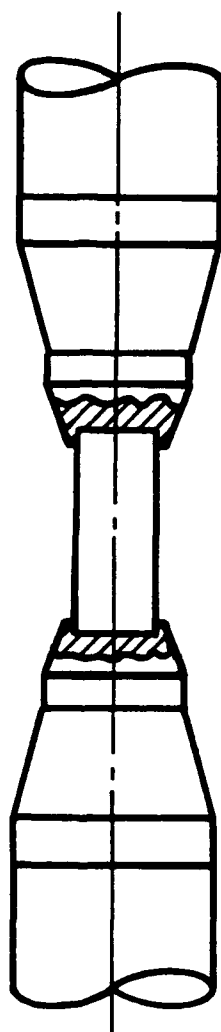


FIGURE 3. Schematic of compression test setup.

Following testing, both partially damaged and totally failed specimens were examined optically while still contained within their transparent Teflon overcoats. Since the experiments were performed under displacement control with radial confinement throughout, even failed specimens remained largely intact. On the other hand, they often fragmented if the coating was removed. In order to prepare the samples for internal scanning electron microscopy (SEM), a small "window" was cut into the Teflon; under vacuum, epoxy mounting resin was able to infiltrate inside the coating, enter the fragmented damage zone, and seal it in place for diamond saw sectioning. These sections were polished, and coated with palladium for SEM study.

III. EXPERIMENTAL RESULTS

Effect of Pressure Deformation and Strength

Shown in Figures 4 - 6 are representative compressive stress- (relative to the hydrostat) strain curves for the three materials, which serve to demonstrate the fundamental variants in their respective behavior. It is useful to consider first that of the matrix alone.

As shown in Figure 4, deformation of the pyroceramic is virtually linear to failure for all conditions, strength increasing with strain rate for both the unconfined and confined states. The ultimate strength also rises with confinement.

This simple pattern is not followed by the composites. For 0°/90° reinforcement (Figure 5), linear stress-strain is observed only for the higher strain rate ($\dot{\epsilon} = 1\text{s}^{-1}$), with ultimate strength rising steadily with confinement. Under quasistatic conditions ($\dot{\epsilon} = 10^{-4}\text{s}^{-1}$), "yielding" occurs prior to failure, with "yield" stress, failure strength, and "ductility" all increasing with confining pressure. Strength is independent of strain rate.

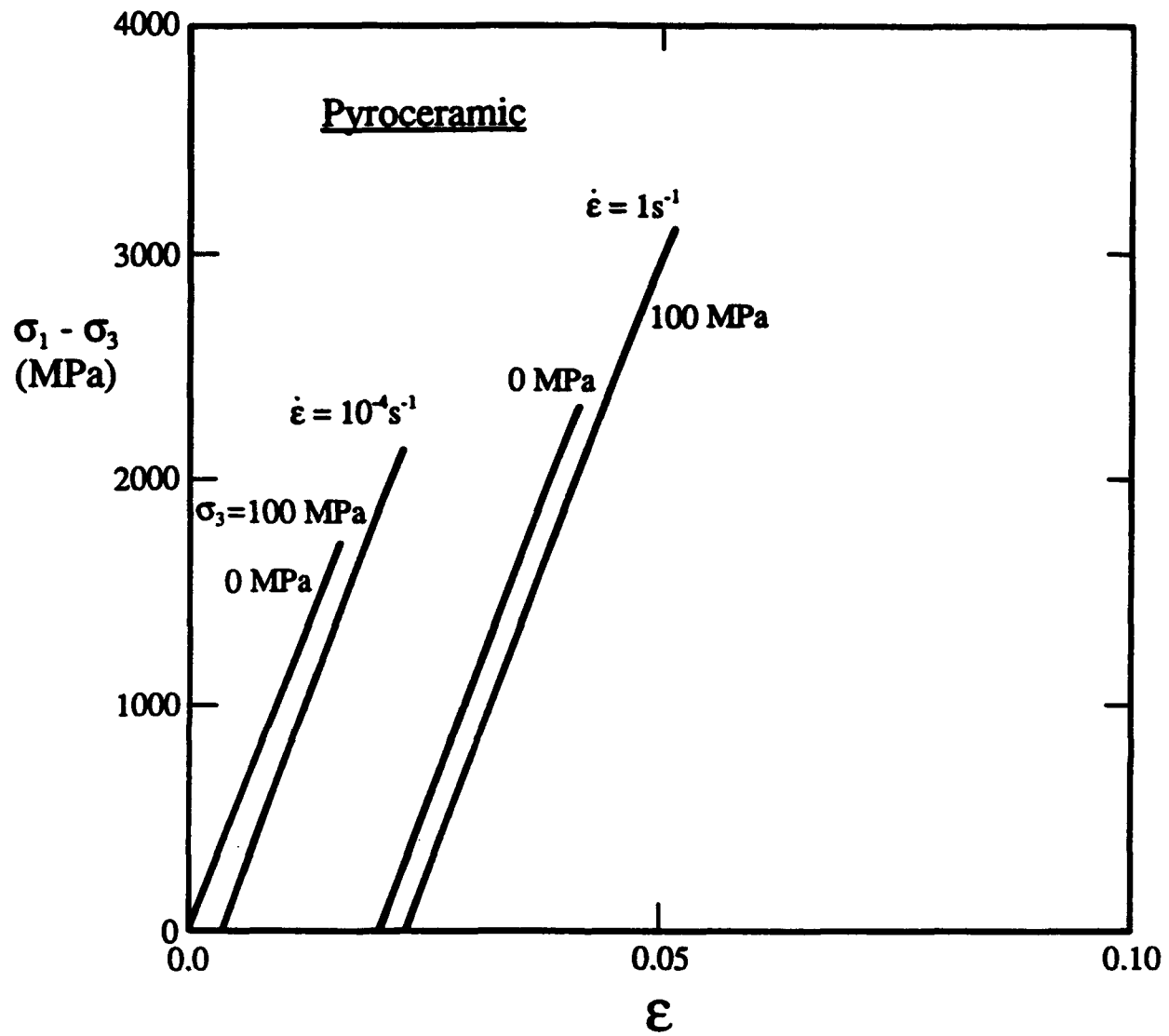


FIGURE 4. Axial stress versus strain for matrix material.

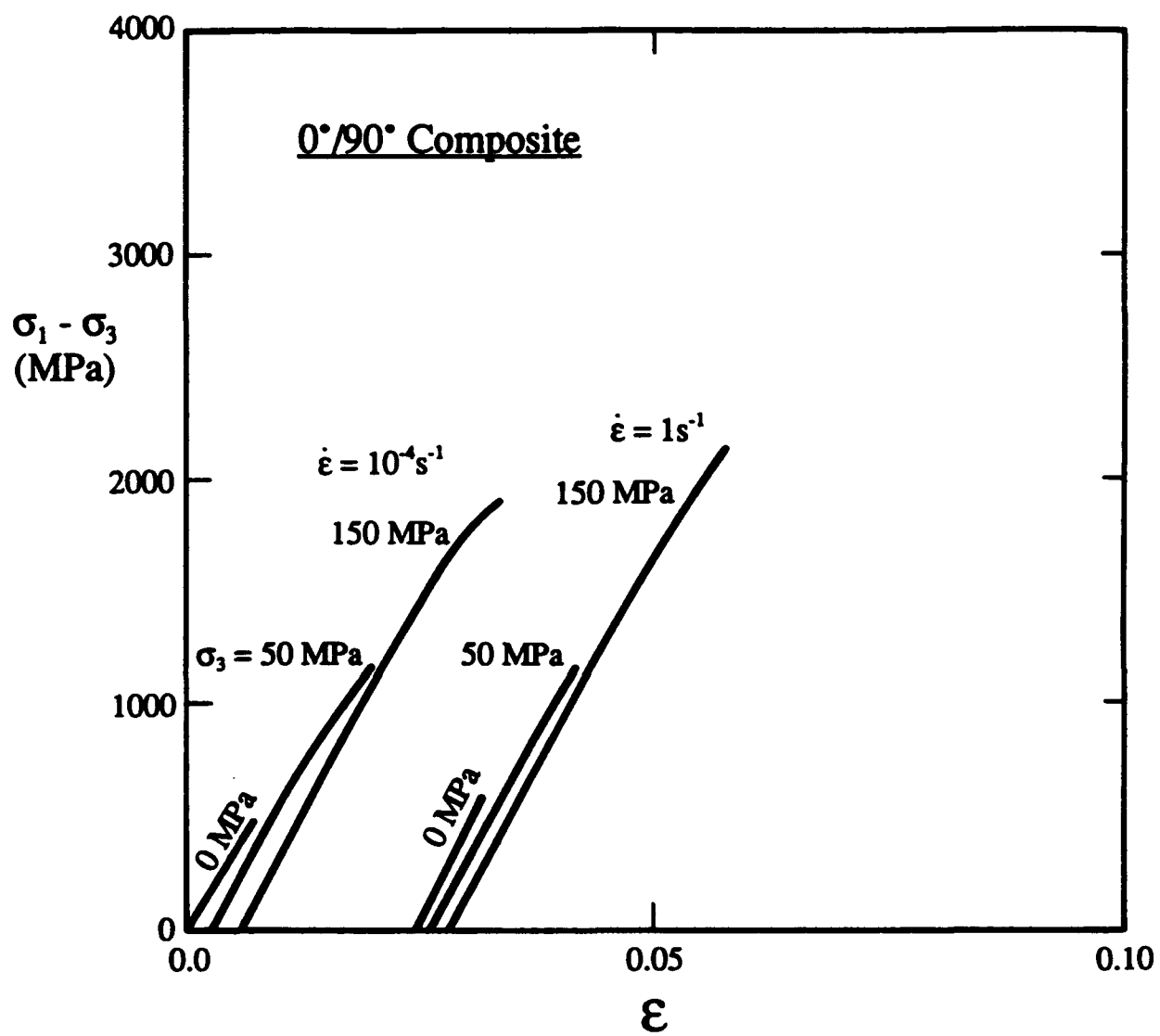


FIGURE 5. Axial stress versus strain for 0°/90° composite.

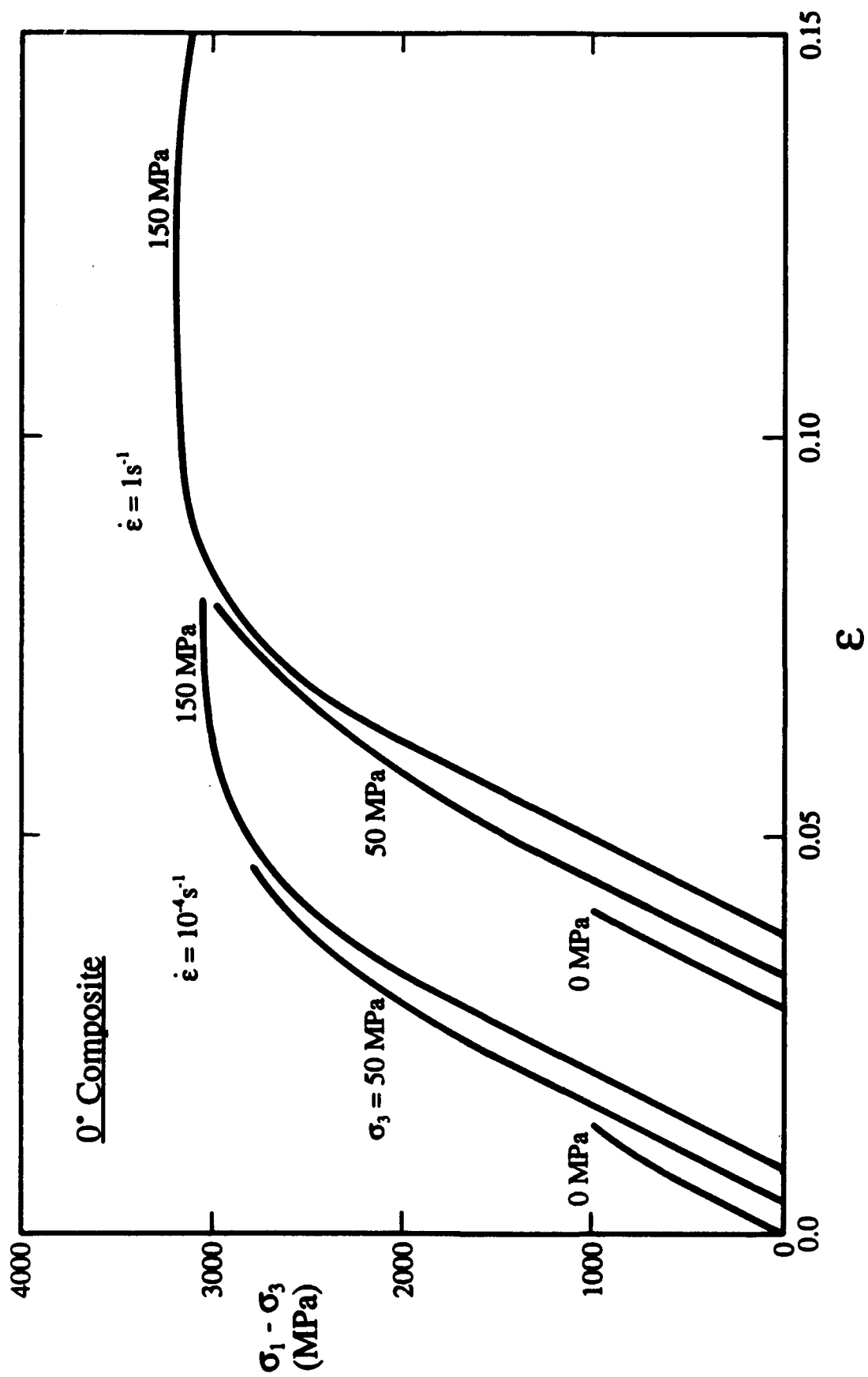


FIGURE 6. Axial stress versus strain for uniaxially reinforced composite.

Uniaxially reinforced pyroceramic "yields" at all strain rates and pressures (Figure 6); "yield" and ultimate strengths again are strain rate independent. However, above some critical value in confining pressure, the ultimate strength becomes virtually insensitive to further increase in confinement.

The influence of pressure on strength is most effectively shown by plotting $\sigma_1 - \sigma_3$ versus σ_3 as discussed earlier. In the case of unreinforced pyroceramic (Figure 7), the strength increases steadily, but at a declining rate with rising confinement, reaching pressure independence at around $\sigma_3 = 200$ MPa. However, the strength curve for $\dot{\epsilon} = 1\text{s}^{-1}$ is elevated from the quasistatic one by a constant factor in σ_3 .

In contrast, little strain rate dependence is observed for the two composite variants (Figures 8 and 9). In the case of the $0^\circ/90^\circ$ material, $\sigma_1 - \sigma_3$ increases monotonically with pressure throughout the range in σ_3 , approaching an apparent asymptotic maximum, while uniaxial reinforcement causes the strength to rise rapidly with pressure and attain a plateau (pressure independence) at around $\sigma_3 = 50$ MPa. It should be noted that over the test range in σ_3 , the differential compressive strength increases by a factor of only 0.3 ($\dot{\epsilon} = 15^{-1}$) to 0.4 ($\dot{\epsilon} = 10^{-4}\text{s}^{-1}$). By contrast, $\sigma_1 - \sigma_3$ for the 0° composite increases by a factor of three, and for $0^\circ/90^\circ$ material by more than four times.

Damage Mechanisms

In the absence of confinement, the pyroceramic fragments at failure into a multitude of microscopic, dust-like particles. With the addition of hydrostatic pressure, failure now occurs via a shear band (Figure 10) usually oriented at an angle of less than 45° relative to the load axis. Closer inspection of the relatively intact zones separated by the fault plane shows them to be riddled with axial microcracks.

In the case of $0^\circ/90^\circ$ composites, failure initiates with axial cracking between adjacent fibers in 90° plies (Figure 11a); the cracks grow subcritically, link up into shear ensembles (arrows, Figure 11b) and lead to 0° ply flexure. Failure finally is reached as the 0° elements within the plies

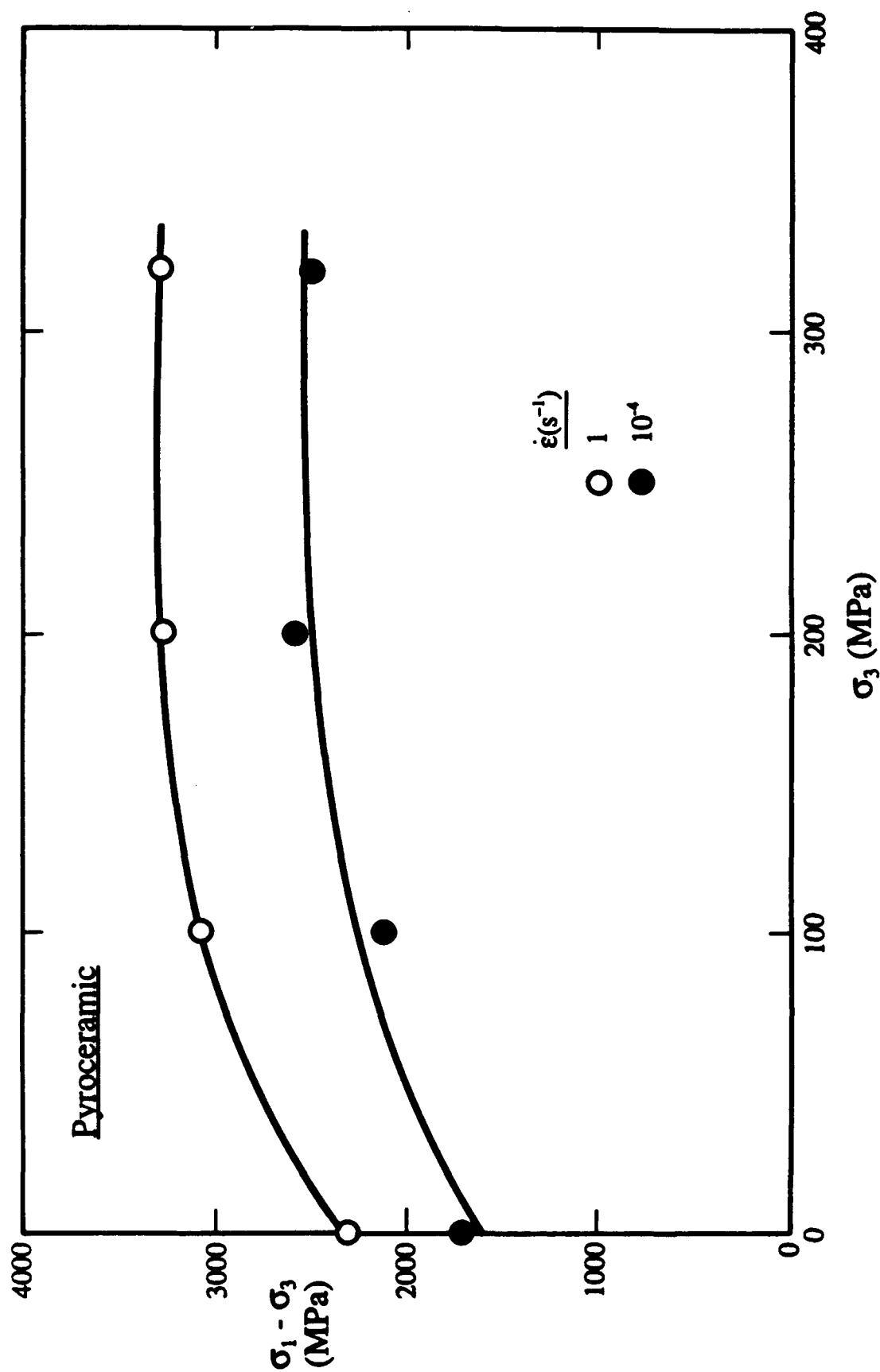


FIGURE 7. Compressive strength of pyroceramic versus confining pressure.

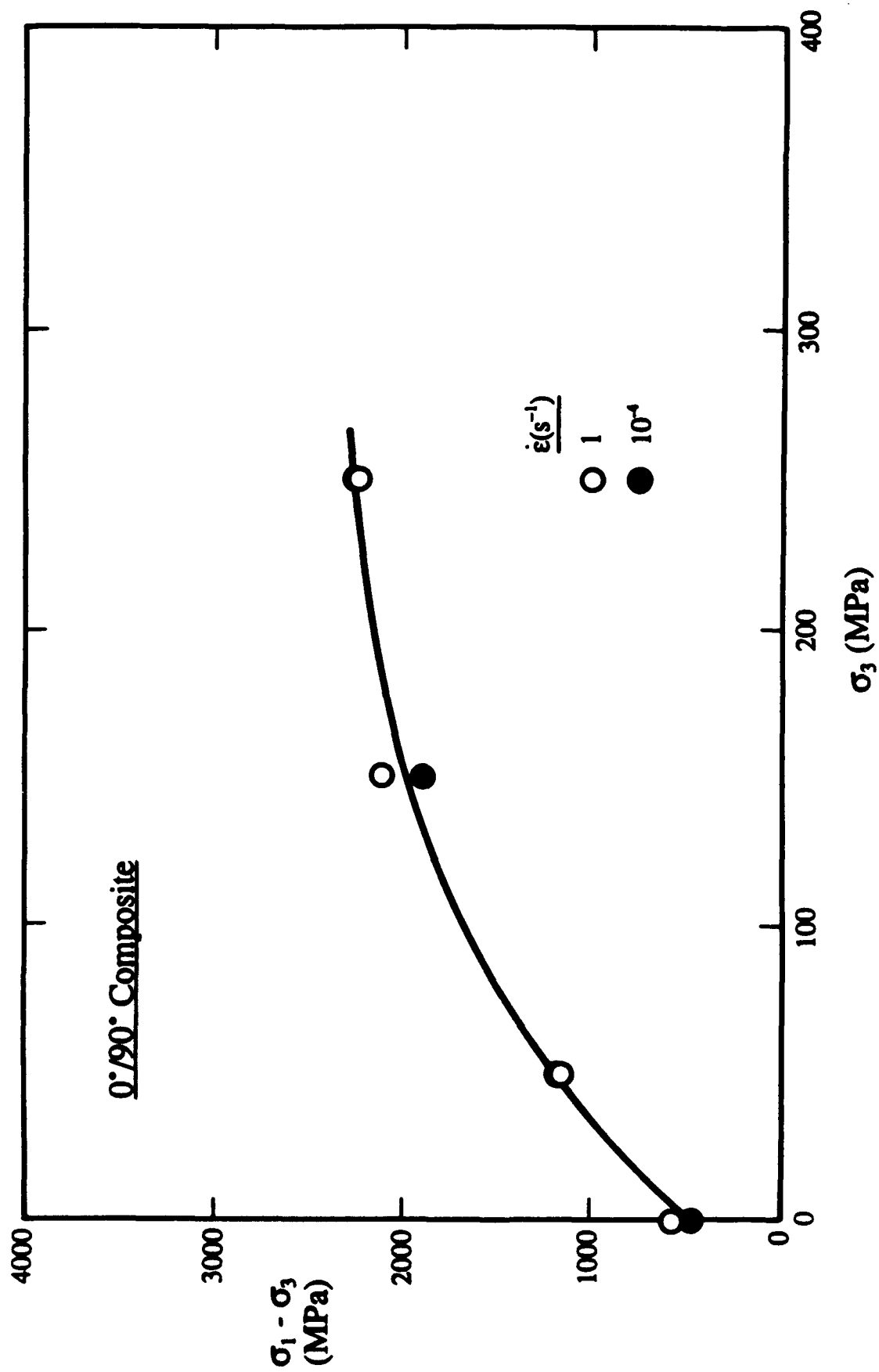


FIGURE 8. Compressive strength of 0°/90° composite versus confining pressure.

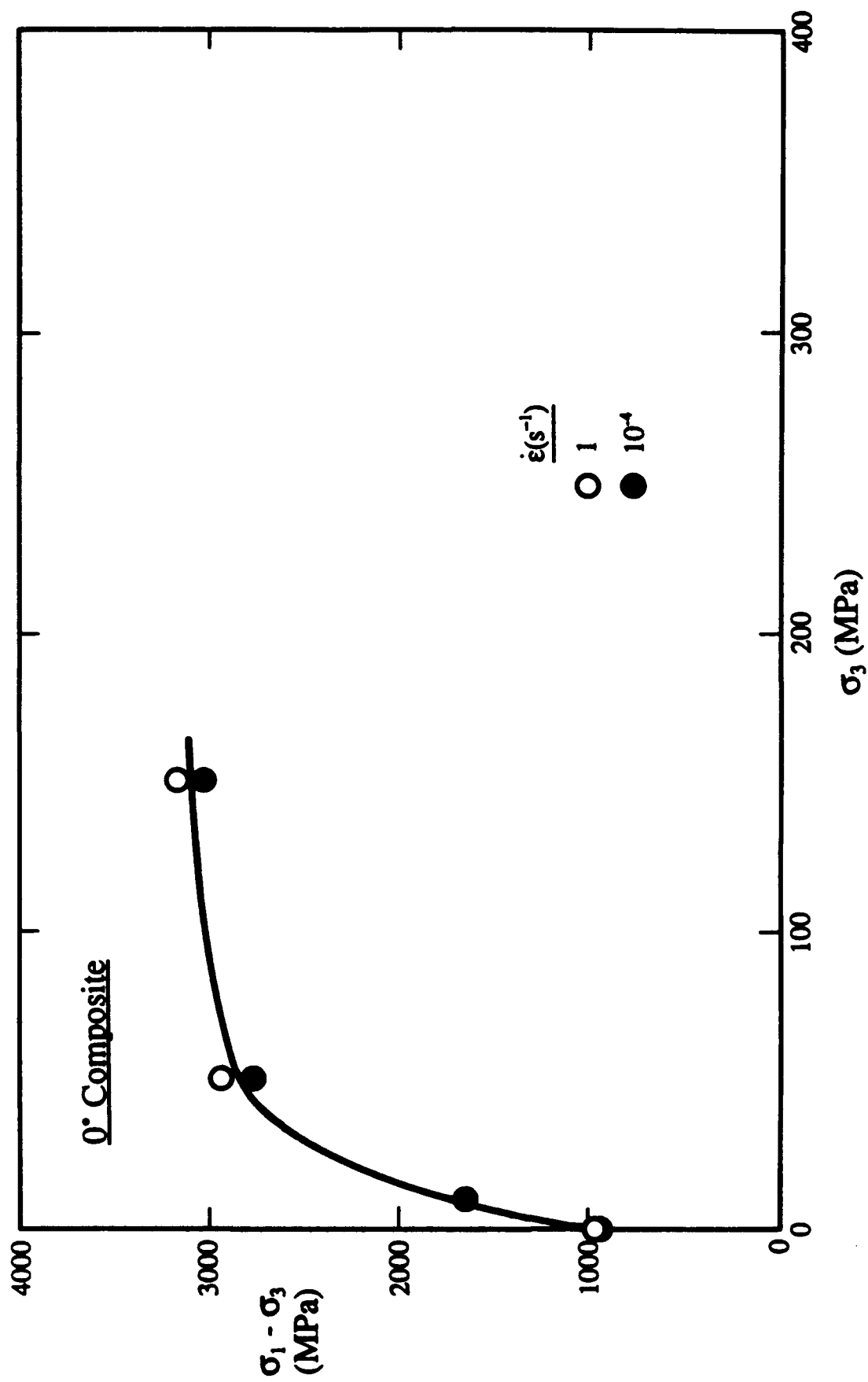


FIGURE 9. Compressive strength of 0° composite versus confining pressure.

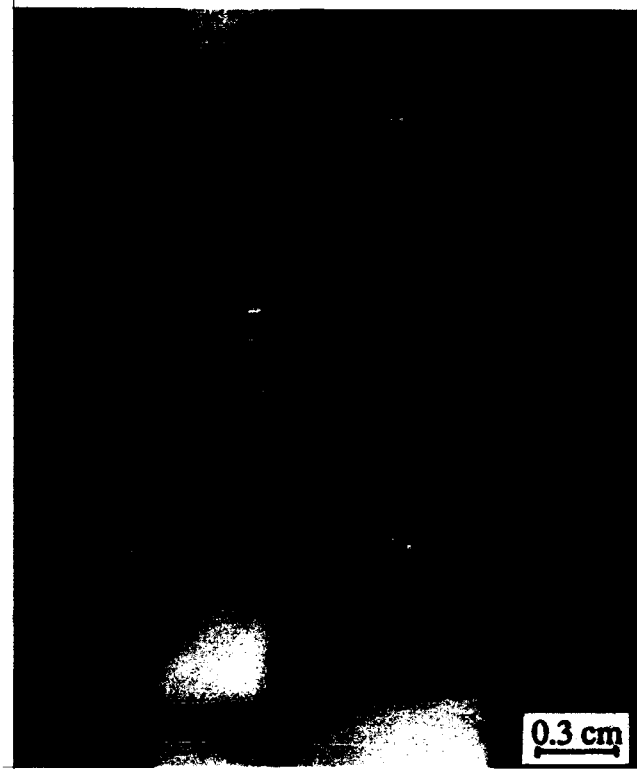
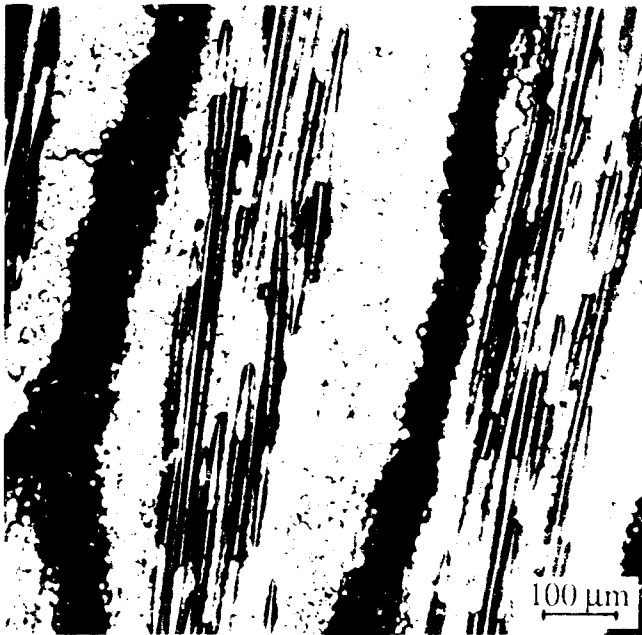
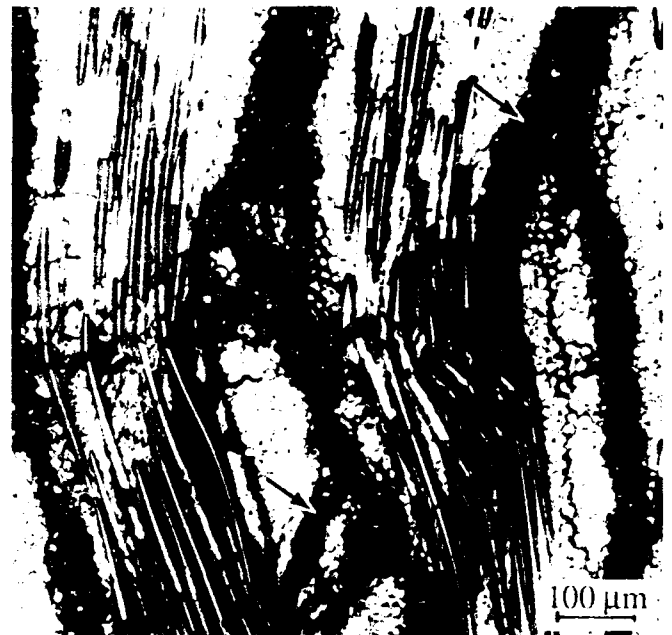


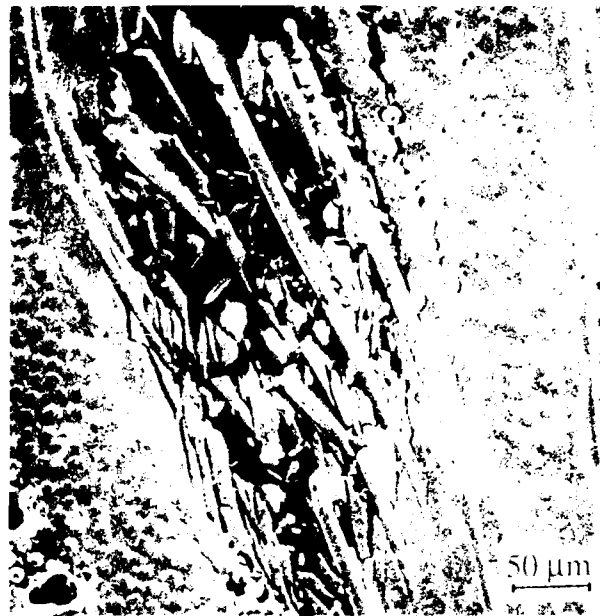
FIGURE 10. Compressive failure of pyroceramic, showing shear band formation; $\dot{\epsilon} = 10^{-4} \text{s}^{-1}$, $\sigma_3 = 200 \text{ MPa}$ (σ_1 vertical).



(a) Axial splitting.



(b) Formation of shear fracture zones (arrows) within 90° plies.



(c) Matrix microfracture at site of 0° ply failure.

FIGURE 11. Compressive failure of 0°/90° composite, $\sigma = 10^5 \text{ psi}$, $G = 0.5G_0$ (vertical).

buckle and induce local fiber fracture and associated matrix microfracture (Figure 11c). It should be noted that until local fine scale matrix fracture occurs, the composite has not failed, but exists in a damaged, but stable, condition. Matrix microfracture represents the loss of fiber stabilization, which takes place by "plastic" flow, *i.e.*, the tiny rubblized fragments slide over one another in order to accommodate the local shear stresses induced by flexed 0° fibers.

At pressures above ambient, the composite fails by forming a shear band at an angle of about 45° (Figure 12a). It appears that no precursory axial splitting (dilatation) is required in order to nucleate the band. Similar behavior is observed for 0° reinforcement, but in this case axial splitting between 0° elements (rather than 90° ones) is the initial step in the (unconfined) failure process. Again the effect of confining pressure is to suppress this dilatational mechanism, so that the failure process is highly localized within a shear zone (Figure 12b), *i.e.*, there is no macroscale dilatation.

Discussion

Both composite variants, as well as the matrix material itself, exhibit behavioral traits which bear qualitative similarities. In particular, they are characterized by early pressure sensitivity, which is eventually lost at higher pressures; these trends correlate with a transition from principally dilatational to shear-type failure modes. Marked variations on this general theme, however, are affected by the specific microstructures, and account for significant quantitative differences.

For the case of the matrix material, it has been shown⁹ that its strain rate sensitivity under ambient conditions is caused by thermally-activated subcritical crack growth. Thus, the same strength differential persists throughout the range of applied confinement (Figure 7), indicating that the pressure effect relates to the suppression of microcrack growth. The latter provides a rationalization for the observed gradual increase in strength with σ_3 , and the approach to an asymptotic level.

In particular, with increasing pressure, the (dilatational) extension of those cracks which are successful in nucleating is made more difficult. Since failure corresponds to the critical combina-



(a) Kink band in 0°/90° composite.



(b) Shear band in 0° composite.

FIGURE 12. Compressive failure modes of composites; $\dot{\epsilon} = 10^{-4} \text{s}^{-1}$, $\sigma_3 = 50 \text{ MPa}$, σ_1 vertical.

tion of crack size and density required to form a shear fault, strength rises with σ_3 . Eventually cracks are nucleated in virtually every grain, at least within local macroscopic enclaves, and the strength saturates at the asymptotic value, since multiple cracking generally will not occur within each grain prior to catastrophic failure.

At higher strain rates, the same saturation in crack density will occur, but the smaller average size of the individual microcracks (due to lower crack extension in the time to reach the failure stress) will correspond to a higher critical shear stress to destabilize the ensemble. Accordingly, the average crack size decrement within roughly the same size crack population will produce a positive and constant strength differential, as measured experimentally.

The behavior of the $0^\circ/90^\circ$ material has a similar dilatational basis, but the scale of events is larger, and probably accounts for the larger relative increase in strength with pressure. As shown in Figure 11, the first stage of failure in this material involves the nucleation of axial interfiber cracks on the scale of the fiber spacing within the 90° laminates; these gradually form shear zones, which nucleate kinking in the 0° plies. With increasing pressure, formation of the precursory axial cracks within the 90° plies is suppressed. This is a classic crack closure effect, whose effectiveness increases with crack size, and apparently is reflected in the steady, four-fold increase in $\sigma_1 - \sigma_3$ with pressure, versus the much smaller (factor of around 0.35) net increase with confinement obtained for the fine-grained pyroceramic. The problem here appears to involve crack nucleation rather than crack growth, since cracks always are observed connecting adjacent fibers, *i.e.*, if they can nucleate, they pop in at a size sufficient to reach the next fiber. Thus, there is no decrement in saturation strength level for different strain rates due to crack growth rate considerations (Figure 8).

Similar axial crack suppression occurs for the uniaxially-reinforced composite, but without the range of 90° fiber ensembles responsible for the observed gradual increase in strength with pressure. Large scale 0° splitting alone is easily suppressed by moderate confinement, and the strength quickly reaches a level that is near constant with further increase in σ_3 .

For both 0° and $0^\circ/90^\circ$ composites, the attainment of a virtually pressure-independent level of strength suggests (recalling Equation 1) the dominance of a shear failure mechanism. With axial splitting, hence 0° buckling, suppressed, the matrix is now generally shielded from microfracture by the strong, axially aligned fibers. However, fiber alignment is not perfect, and local kinking can occur due to fiber misalignment (as much as five degrees). Such kinks have been observed in polymeric composites under hydrostatic pressure, accommodated by matrix yielding.⁵ In the latter case, local matrix microfracture would be required at the sites of misalignment, where fiber shielding necessarily would be less effective. Because of this requirement for matrix accommodation, dilatation will remain a factor, probably accounting for the fact that for both composites, there remains some tendency for strength to increase slightly with σ_3 even at the higher test pressures.

IV. ACKNOWLEDGEMENTS

The support of the Office of Naval Research under Contract Number N00014-92-C0093 is gratefully acknowledged. Careful experimental work by, and helpful discussions with, Mr. A. Nicholls are greatly appreciated.

V. REFERENCES

1. "Temperature, Strain Rate, and Fiber Orientation Effects in the Fracture of a SiC Fiber-Reinforced Glass Matrix Composite," by J. Lankford, *Composites*, **18** pp. 145, 1987.
2. M. L. Wilkins, "Mechanics of Penetration and Perforation," *Int. J. Eng. Sci.*, **16** (1978) 793-807.
3. H. C. Heard and C. F. Cline, "Mechanical Behavior of Polycrystalline BeO, Al₂O₃ and AlN at High Pressure," *J. Mat. Sci.*, **15** (1980) 1889-1897.

4. G. R. Johnson, T. J. Holmquist, J. Lankford, C. E. Anderson, and J. Walker, "A Computational Constitutive Model and Test Data for Ceramics Subjected to Large Strains, High Strain Rates, and High Pressures," Final Report DARPA Contract No. DE-AC04-87AL-42550, August 1990.
5. J. Lankford, "The Compressive Failure of Polymeric Composites Under Hydrostatic Confinement," *J. Mat. Sci.* (submitted).
6. "Compressive Fracture Processes in an Alumina/Glass Composite," by R. Arrowood and J. Lankford, *Journal of Materials Science*, **22** pp. 3737, 1987.
7. "Strength of Monolithic and Fiber-Reinforced Glass Ceramics At High Rates of Loading and Elevated Temperature," by J. Lankford, *Ceramic Engineering and Science Proceedings*, **9** pp. 843, 1988.
8. C. W. Weaver and J. G. Williams, "Deformation of a Carbon-Epoxy Composite Under Hydrostatic Pressure," *J. Mat. Sci.*, **10** (1975) 1323-1333.
9. "Dynamic Compressive Fracture in Fiber-Reinforced Ceramic Matrix Composites," by J. Lankford, *Materials Science and Engineering*, **A107**, pp. 261, 1989.

IV.

**TESTING OF HIGH STRENGTH CERAMICS
WITH THE SPLIT HOPKINSON PRESSURE BAR**

by

**J. M. Staehler, W. W. Predebon, B. J. Pletka
Michigan Technological University
Houghton, MI 49931**

and

**J. Lankford
Southwest Research Institute
San Antonio, TX 78228**

ABSTRACT

The split Hopkinson pressure bar was used to study the failure of a high strength alumina at strain rates on the order of 10^3 sec^{-1} . There appears to be a critical strain rate above which the traditional method of using the transmitter bar signal to calculate the stress in the specimen is no longer valid. To compute the correct stress in the specimen it was necessary to use the strain signal from a gage mounted directly on the specimen.

I. INTRODUCTION

The split Hopkinson pressure bar (SHPB) has been used extensively in the past¹ to study the deformation of metals at strain rates of the order of 10^3 sec^{-1} . More recently this technique has been used in the study of deformation and fracture of ceramics.^{2,3} Figure 1 is a schematic of the device showing the specimen as it is positioned between the two elastic pressure bars. The striker bar is propelled toward the incident bar and an elastic compressive wave is generated by the impact that is partially transmitted into the specimen and partially reflected at the incident bar/specimen interface. The strain gage on the incident bar is used to measure both the strain due to the incident wave as well as that due to the reflected wave. The strain gage mounted on the transmitter bar measures the strain due to the wave which is transmitted across the specimen/transmitter bar interface.

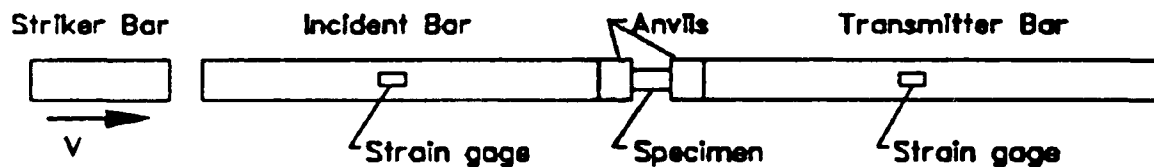


FIGURE 1. Schematic diagram of split Hopkinson pressure bar.

If the specimen is short and the stress is assumed to be uniform along its length, then the strain and average stress in the specimen are¹

$$\epsilon_s = -\frac{2C_o}{l_o} \int_0^t \epsilon_r dt' \quad (1)$$

$$\sigma_s = E \left(\frac{A}{A_s} \right) \epsilon_t \quad (2)$$

where

- c_o = elastic wave velocity in the bar
- l_o = initial specimen length
- E = Young's modulus of the transmitter bar
- A/A_s = ratio of bar and specimen areas, respectively
- t = time
- ϵ_r = the reflected strain in the incident bar
- ϵ_t = the strain in the transmitter bar

Understanding the deformation and fracture characteristics of ceramics at high strain rates is relevant from both a fundamental and practical (*e.g.*, armor protection) viewpoint. Consequently, it is imperative that the testing procedure used be appropriate for the small strains, low fracture toughness, and high strengths that can be achieved in some ceramics. The purpose of this communication is to demonstrate that, depending on the magnitude of the strain rate, modifications are necessary to the traditional method of calculating stresses with the SHPB. When testing very high strength, low ductility ceramics at very high strain rates in the SHPB, the stress in the specimen cannot be determined from Equation 2. The reason for this behavior is not fully understood at this time. It is under investigation and will be the subject of a latter paper.

II. EXPERIMENTAL PROCEDURE

The aluminas tested were fabricated at Michigan Technological University (MTU) by vacuum hot pressing and hot isostatic pressing a high purity powder. Test specimens were machined to 4.76 mm Dia. x 9.52 mm long cylinders ($L/D = 2$) to the tolerances used previously.^{2,3} In contrast to the traditional SHPB technique, strain gages (1.57 mm gage length) were mounted directly to each specimen to measure axial strain. Anvils the same diameter as the bars were placed on either side of the specimen.* The anvil material was either a Coors AD999 alumina, an MTU alumina, or tungsten carbide. The benefit of using alumina anvils (in addition to protecting the ends of the incident and transmitter bars) was that the acoustic impedance of alumina is almost identical to that of steel. For this reason, no correction for impedance was needed when analyzing the signals in either the incident or transmitter bars. It was still necessary to correct for the change in diameter of the specimen as shown in Equation 2.

The bars were calibrated in a manner consistent with that discussed elsewhere.¹ The data from an actual test included recordings of the incident, transmitter, and specimen strain gage outputs.

III. RESULTS AND DISCUSSION

Stress and strain histories for two SHPB tests are shown in Figures 2 and 3; both tests were performed on a high strength MTU alumina using alumina anvils. The stress signals are based on the transmitter bar strain signals and Equation 2 while the strain signals came directly off of the strain gaged specimens. The slopes of the strain signals in Figures 2 and 3 yield specimen gage

* Tests were performed at Southwest Research Institute using their SHPB facilities; both the incident and transmitter bars were 12.25 mm in diameter and 111.76 cm in length.

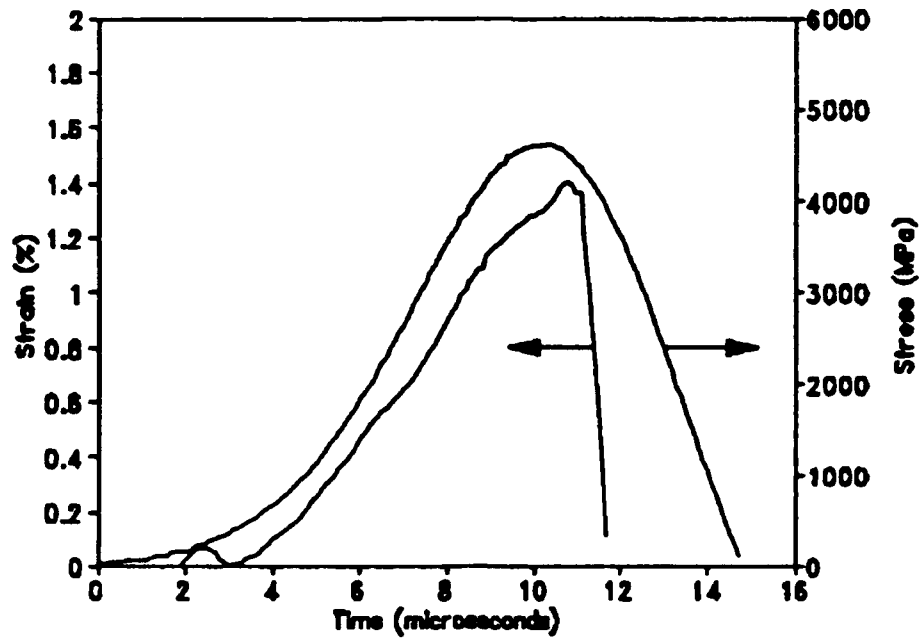


FIGURE 2. Compressive stress and strain signals from SHPB test of MTU alumina. Stress signal was calculated from equation 2 and strain signal came from specimen gage.

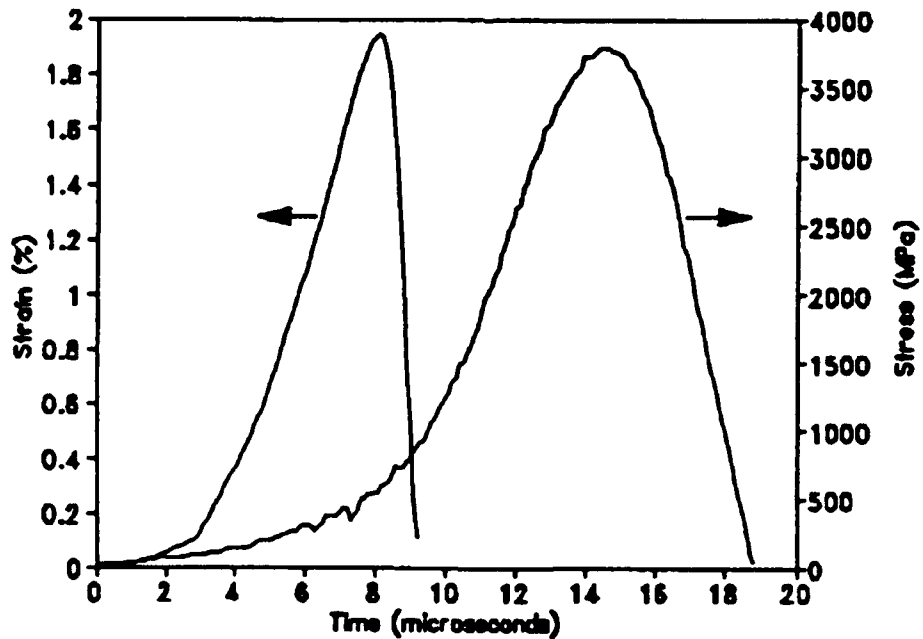


FIGURE 3. Compressive stress and strain signals from SHPB test of MTU alumina. Stress signal was calculated using equation 2 and strain signal came from specimen strain gage.

based strain rates ($\dot{\epsilon}_g$) of about 2300s^{-1} and 4600s^{-1} , respectively. The difference in strain rates is mainly due to the difference in striker bar velocities; the test shown in Figure 3 had a higher velocity than the one in Figure 2.

If the stresses in Figure 2 are divided by Young's modulus (413 ± 20 GPa, determined from quasistatic and ultrasonic testing), the result is the stress-derived strain signal of Figure 4. The slope of the central portion of this curve gives a stress based strain rate ($\dot{\epsilon}_s$) of 2100s^{-1} , which is within 10% of the strain rate from Figure 2. The strain signal from Figure 2 is repeated in Figure 4 for comparison. The peak stress in the specimen using the specimen gage output and Young's modulus was 4900 MPa, again within 10% of the 4500 MPa indicated by the stress pulse.

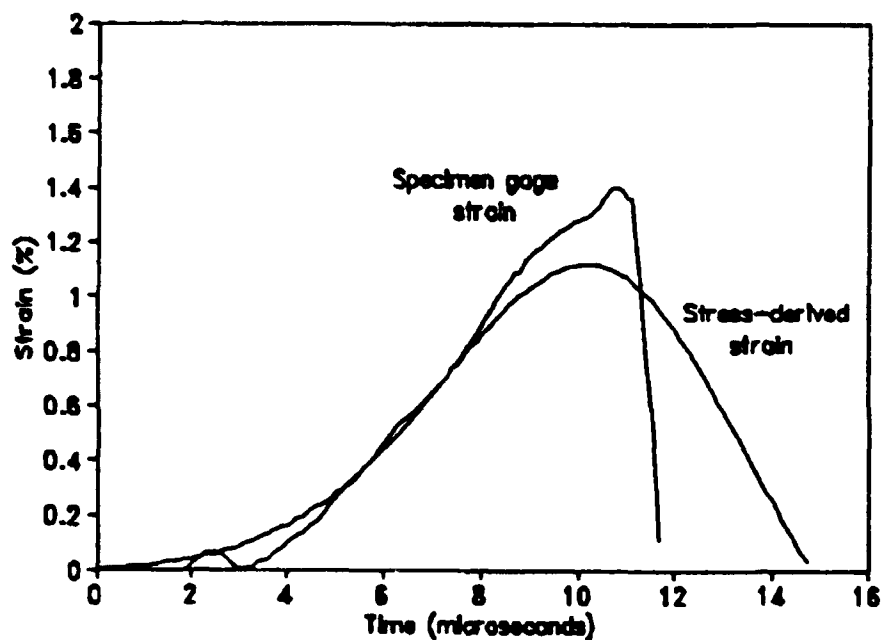


FIGURE 4. Comparison of stress-derived strain and specimen strain gage signal for the low strain rate test of Figure 2.

When a similar analysis was performed on the stress signal of Figure 3, the results were quite different. Noting that the strain signal of Figure 3 peaks in about $7.5\ \mu\text{s}$ compared with $14.5\ \mu\text{s}$ for the stress pulse, this was not surprising. The stress-derived strain signal for this test is shown in Figure 5. This strain signal differs significantly from the specimen strain gage output. The strain gage-derived strain rate of 4600s^{-1} from Figure 3 was significantly higher than the 1800s^{-1} calculated from the stress-derived strain signal of Figure 5. In addition, the peak stress in the specimen using the peak strain of Figure 3 and Young's modulus was about $8000\ \text{MPa}$, over twice the value of $3800\ \text{MPa}$ suggested by the stress pulse in this same figure.

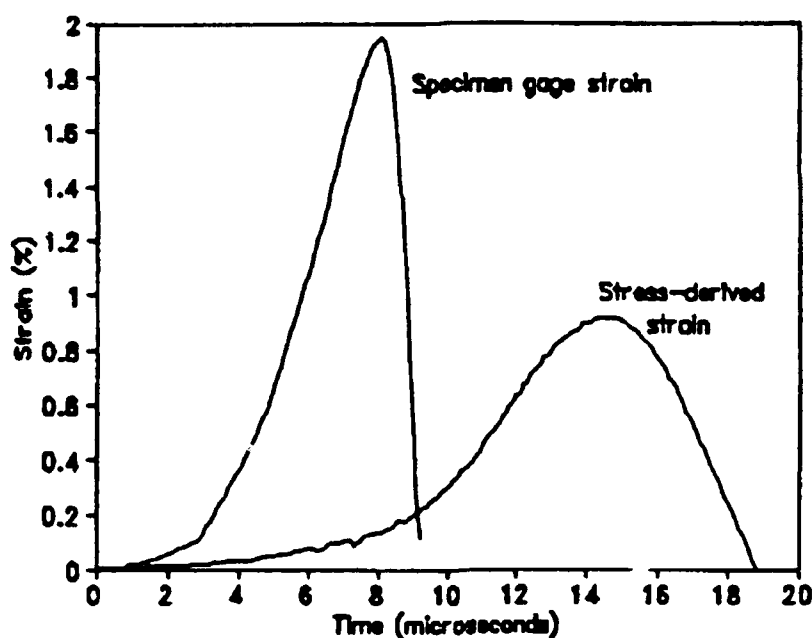


FIGURE 5. Comparison of stress-derived strain and specimen strain gage signal for the high strain rate test of Figure 3.

These results suggest that at the higher strain rates wave dispersion may be compromising the transmitter bar strain gage signal; clearly this would compromise the computed ultimate strength as well. Further evidence for this conclusion is shown in Figure 6.

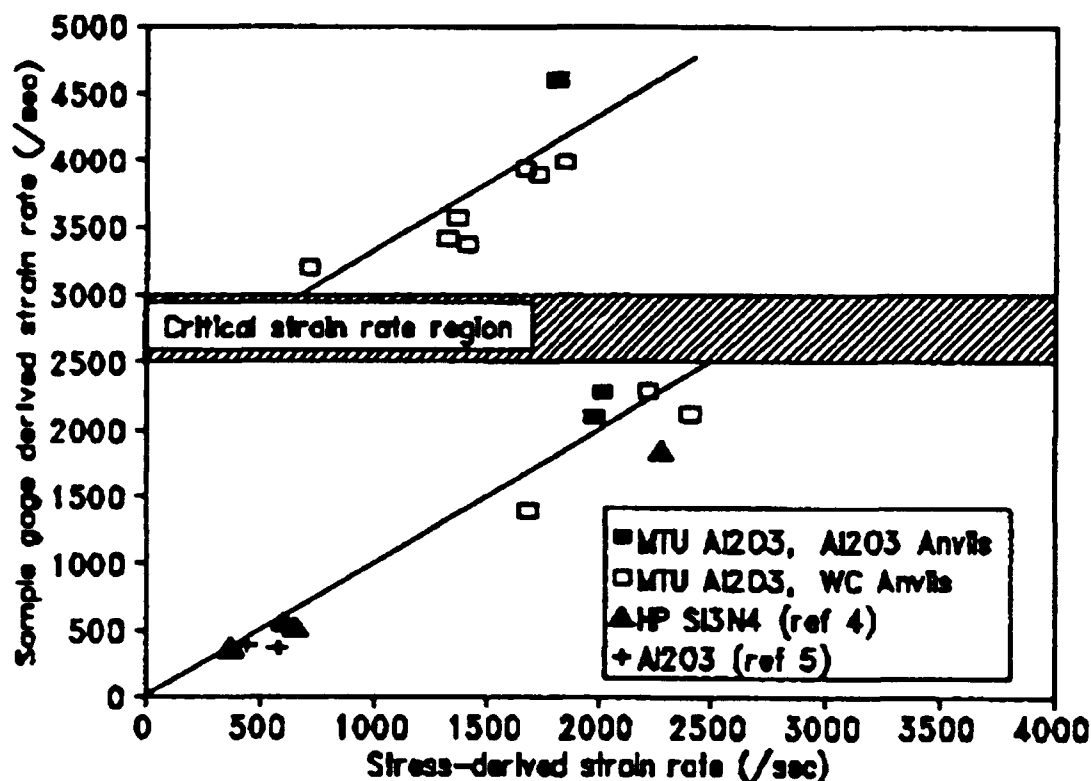


FIGURE 6. Comparison of specimen gage-derived strain rates and stress-derived strain rates for a number of tests.

In Figure 6, $\dot{\epsilon}_g$ and $\dot{\epsilon}_s$ are plotted versus one another for a number of compression tests, including a few involving hot pressed Si_3N_4 and a weaker alumina.⁵ The results fall into two groups: one in which the data cluster about $\dot{\epsilon}_g = \dot{\epsilon}_s$, and the other for which $\dot{\epsilon}_g > \dot{\epsilon}_s$. The transition between the data sets occurs at a critical strain rate, which evidently corresponds to some kind of wave velocity discontinuity. The critical event does not appear to be stress related, since the dif-

ference between $\dot{\epsilon}_{sg}$ and $\dot{\epsilon}_{sr}$, normalized by either, is stress independent. It is clear, however, that the peak stress (compressive strength) disparity derived from Figure 3 (3800 MPa versus 8000 MPa) arises directly and solely from the variance between the strain-time response of the specimen and the transmitter bar strain gage response.

These results are consistent with the recent SHPB work on magnesium-partially stabilized zirconia (Mg-PSZ).⁶ There it was argued that the small strains incurred in a ceramic material prior to failure necessitated the use of strain gages mounted directly to the specimen. However, it was noted that the average stress in the specimen could still be calculated using the transmitter bar signal and Equation 2. Using this stress, combined with the strain signal from the specimen over the linear elastic range, the authors were able to reproduce to within 5%, Young's modulus for the Mg-PSZ from ultrasonic tests. This is consistent with the alumina tests discussed previously because the MG-PSZ tests were performed at very low strain rates where the results in Figures 4 and 6 suggest that the alumina data would agree as well.

Although the two tests shown in Figures 2 and 3 were conducted using alumina anvils, the majority of the MTU alumina tests in Figure 6 were performed using WC anvils. This was necessary because the AD999 anvils broke during the test. Due to the impedance mismatch between the WC, the steel bars, and the alumina specimens, some wave reflections must occur at all dissimilar interfaces. This would account for some of the disparity between the stress-derived strains and the specimen gage strains. However, even allowing for the need for a wave reflection correction, Figure 6 suggests that there is still a critical strain rate above which the transmitter bar signal cannot be used.

Implicit in the construction of Figures 4 and 5 was the assumption that the specimens remained essentially elastic during the tests. This was felt to be a reasonable assumption for this alumina at room temperature for two reasons. First, from quasistatic and intermediate strain rate tests (10^{-4} to 10^0 sec^{-1}), this material exhibited a linear stress-strain response up to about 1.8% strain

and subsequent catastrophic failure. Secondly, quasi-static and intermediate strain rate testing has shown⁷ that the fracture stress rises gradually with strain rate, reaching about 7500 MPa at 100 sec^{-1} . If the average stress in Figure 3 was indicative of the true fracture strength at a strain rate of 10^3 sec^{-1} , this general trend of increasing strength with strain rate would show a significant reversal; such a reversal seems unlikely.

IV. CONCLUSIONS

Testing of high strength, low ductility ceramics such as alumina at high strain rates using the SHPB will require modification to the conventional method in which stresses are calculated. For tests above about 2700 s^{-1} , the stress, strain, and strain rate of the specimen cannot be calculated from the transmitter bar signal. It is necessary to calculate the stress in the specimen using the strain signal obtained from a gage mounted directly to the specimen and Young's modulus from quasi-static tests. This method should be valid provided there is negligible macroscopic plastic deformation preceding failure. Had the traditional method been used, the apparent compressive fracture stress at high strain rates would have been as much as 50% lower. The reason for this problem remains unclear at this time and is under investigation. At lower strain rates it appears that the transmitter bar does provide reasonable results.

V. ACKNOWLEDGMENTS

The authors would like to thank Mr. Arthur Nicholls of Southwest Research Institute for his discussion and efforts in conducting the SHPB tests. This research was supported by Alliant Techsystems Inc. (formally Honeywell), ALCOA Foundation, the College of Engineering of Michigan Technological, and the Office of Naval Research through Contract No. N0014-92-C-0093.

VI. REFERENCES

1. U. S. Lindholm, "Some Experiments With the Split Hopkinson Pressure Bar," *J. Mech. Phys. Solids*, **12**, 317-335 (1964).
2. J. Lankford, "Compressive Strength and Microplasticity in Polycrystalline Alumina," *J. Mater. Sci.*, **12** [4] 791-796 (1977).
3. J. Lankford, "Uniaxial Compressive Damage in α -SiC at Low Homologous Temperatures," *J. Am. Ceram. Soc.*, **62** [5-6] 310-312 (1979).
4. J. Lankford, unpublished data (1992).
5. A. Cosculluela, J. Cagnoux, and f. Collombet, "Uniaxial Compression of Alumina: Structure, Microstructure, and Strain Rate," *J. de Physique IV*, Colloque C3, suppl. au *J. de Physique III*, **1**, 109-116, (1991).
6. W. P. Rogers and S. Nemat-Nasser, "Transformation Plasticity at High Strain Rate in Magnesia-Partially-Stabilized Zirconia," *J. Am. Ceram. Soc.*, **73** [1] 136-139 (1990).
7. J. M. Staehler, W. W. Predebon, and B. J. Pletka, "A High Purity Alumina With Exceptional Compressive and Flexure Strength Behavior or Alumina Revisited - But much Better Than Ever," Proceedings, 1991 Army Symposium on Solid Mechanics, Plymouth, MA, Nov 4-7, 1991 (in print).